RAMAN SPECTROSCOPY APPLICATIONS IN AGRICULTURE: FROM

EARLY PLANT STRESS DIAGNOSTICS TO ANIMAL DIET PREDICTIONS

A Dissertation

by

NARANGEREL ALTANGEREL

Submitted to the Office of Graduate and Professional Studies of
Texas A&M University
in partial fulfillment of the requirements for the degree of

DOCTOR OF PHILOSOPHY

Chair of Committee,	Marlan O. Scully
Committee Members,	William Bassichis
	Joshua Yuan
	Aleksei M. Zheltikov
Head of Department,	Peter McIntyre

December 2017

Major Subject: Applied Physics

ABSTRACT

This work is mainly devoted to development of Raman spectroscopic techniques for *in vivo* detection of abiotic plant stress and animal diet prediction by Raman spectra of their feces. The ability to measure plant stress *in vivo* responses is becoming increasingly vital as we consider human population growth and climate change reports. In the first study, Raman spectroscopy was utilized to nondestructively detect abiotic stress responses during 48 hours of plant response to multiple stresses. Coleus *Solenostemon scutellarioides* plants were subjected to four common abiotic stress conditions, individually: high soil salinity, drought, chilling exposure, and light saturation and examined post stress induction by Raman microscopic and spectroscopic systems, and chemical analytical methods. While anthocyanin levels increased, carotenoid levels decreased under exposure to these stress conditions by *in vivo* Raman measurements and the chemical analysis. This unique negative correlated relationship shows that plant stress response is fine-tuned to protect against stress-induced damage. In the next study, we utilized a Raman spectroscopy as detection tool to predict cow diets by their feces. The objective of this study was to compare near infrared reflectance spectroscopy (NIRS) to Raman spectroscopy of fecal samples for predicting the percentage of Honey mesquite *Prosopis glandulosa Torr.* in the diet of ruminally fistulated cattle fed three different base hay diets and to compare them for their ability to discriminate among the three base diets. Spectra were collected from fecal materials from a feeding trial with mesquite fed at 0, 1, 3 and 5% of the diet and base hay diets of timothy hay *Phleum pratense L.*, Sudan hay *Sorghum sudanense (Piper) Stapf*, or a 50 : 50 combination of Bermudagrass hay *Cynodon dactylon (L.) Pers.* and beardless wheat hay *Triticum aestivum L.*.

NIRS and Raman spectra were used for partial least squares regression calibrations with the timothy and Sudan hays and validated with the Bermudagrass beardless wheat hay diets. NIRS spectra provided useful calibrations (R^2=0.88, slope=1.03, intercept=1.88, root mean square error=2.09, bias=1.95, ratio of performance to deviation=2.6), but Raman spectra did not. Stepwise discriminant analysis was used to select wavenumbers for discriminant among the three hays. Fifteen of 350 possible wavenumbers for NIRS spectra and 29 of 300 possible wavenumbers for Raman spectra met the $P \leq 0.05$ entry and staying criteria. Canonical discriminant analysis using these wavenumbers resulted in 100% correct classification for all three base diets and the Raman spectra provided greater separation than NIRS spectra. Discrimination using Raman spectra was primarily associated with wavenumbers associated with undigestible constituents of the diet, i.e., lignin. In contrast, discrimination using NIRS spectra was primarily associated with wavenumbers associated with digestible constituents in the diet, i.e., protein, starch and lipid. At last, coherent Raman scattering spectroscopy is studied specifically, with the Gaussian ultrashort pulses as a hands-on elucidatory extraction tool of the clean coherent Raman resonant spectra from the overall measured data contaminated with the non-resonant four wave mixing background. The integral formulae for both the coherent anti-Stokes and Stokes Raman scattering are given in the semiclassical picture, and the closed-form solutions in terms of a complex error function are obtained. An analytic form of maximum enhancement of pure coherent Raman spectra at threshold time delay depending on bandwidth of probe pulse is also obtained. The observed experimental data for pyridine in liquid-phase are quantitatively elucidated and the inferred time-resolved coherent Raman resonant results are reconstructed with a new insight.

DEDICATION

To my kids, Gonchi and Yanichka

ACKNOWLEDGEMENTS

CONTRIBUTORS AND FUNDING SOURCES

NOMENCLATURE

CCD   Charge-Coupled array Detector

2D   Two Dimension

3D   Three Dimension

NIRS   Near Infrared Spectroscopy

f.NIRS   Fecal Infrared Spectroscopy

CARS   Coherent Anti-Stokes Raman Spectroscopy

CSRS   Coherent Stokes Raman Spectroscopy

ROS   Reactive Oxygen Species

DM   Dry Matter

NDF   Neutral Detergent Fiber

ADF   Acid Detergent Fiber

BW   Bermudagrass hay and beardless Wheat hay

WN   Wavenumber

TABLE OF CONTENTS

LIST OF FIGURES

LIST OF TABLES

INTRODUCTION

Motivation and Research Objective

The Green Revolution has given us the ability to feed our hungry world. But with the ever increasing world population and decreasing arable land we will not be able to feed ourselves in the near future. We clearly need agricultural innovation(s) to forestall this disaster. Early detection of plant stress is one such tool for optimizing crop yields. Current in vivo sensing technologies are limited by the time it takes to detect a stress response, the types of stress factors that can be examined, and the level of the stress or the physiological changes that are detectable. Here Raman spectroscopy is shown for the first time to detect abiotic stress responses within 48 hours for multiple stress factors. Anthocyanin, a known reactive oxygen scavenging (ROS) molecule was shown to increase within 36 hours of exposure to cold, excess light, saline and drought stress conditions. Conversely, carotenoid levels were shown to decrease. The two pigments were anti-correlated across all four abiotic stress factors. This unique anti-correlation, which has never been demonstrated before, indicates that the stress response is fine tuned to protect against stress induced damage. In principle, early detection of the anthocyanin/carotenoid stress response would allow for intervention to improve crop yields and avoid seasonal crop failures. Non-destructive stress detection using Raman Spectroscopy holds promise for increasing agricultural production and will speed up the development of selective breeding programs for stress resistant strains of commercially important food crops.

Background

Raman Effect

There are two types of light scattering due to interaction of light with matter: elastic (Rayleigh scattering) or inelastic (Raman scattering). Though inelastic scattering of light by matter was predicted by Smekal in 1923, it was first observed in experimentation by Raman and his collaborator K.S.Krishnan in 1928 [1]. For the discovery of the effect, which was named after him, Raman won a Nobel Prize in 1930. The Raman effect (or scattering) is caused by the interaction between vibrational/rotational motions of molecules with electromagnetic radiation. Rayleigh scattering (Figure 1.1) is elastic scattering that takes place with no loss of energy or frequency change - it is most of the scattering that occurs when light shines on a sample. Raman scattering, on the other hand, is spurred by inelastic scattering of
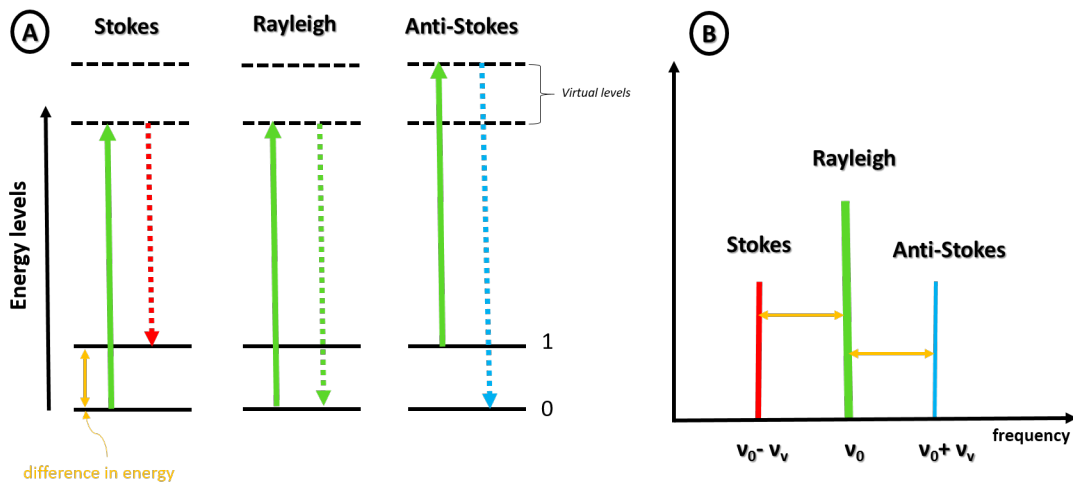
Figure 1.1: A) The energy level diagram of Rayleigh and Raman processes, B) Raman and Rayleigh scatterings of excitation at a frequency ν_0 and molecular vibration in the sample of frequency ν_v
.

the incident photons, since energy transferred to or received from the sample due to changes in the vibrational/rotational modes of sample molecules cause changes in the frequency of the scattered light. Incident photons that give up energy to the sample are scattered with a red shifted frequency and called a stokes shift (Figure 1.1A). If an already excited molecule gives energy to a scattered photon, the output has a blue-shifted frequency, and is referred to as anti-Stokes shift (Figure 1.1A). However, because the probability of a molecule being in an excited state is much lower than being in the ground state, the anti-Stokes shift happens less often than the Stokes-shift. The Raman scattering photons usually analyzed are Stokes photons, or Stokes lines. Though the lack of anti-stokes photons causes weak anti-stokes lines, the absence of fluorescence interference (an issue for stokes photons) drive them to at times be favored in analysis. Fluorescence is very different from Raman scattering. The excitation light is completely absorbed by the molecule during fluorescence process and it results an electronic energy state change (Figure 1.2). Raman scattered light is released instantaneously, while fluorescent light is later released during the molecule relaxes back to a lower energy state [2]. Raman scattering is determined by electrical polarizibility changes during the vibration, whereas another vibrational technique of infrared (IR) detects vibrations when the electrical dipole moment changes [3]. IR process requires the frequency of excitation light has to match the energy differences between ground and excited vibrational states (Figure 1.2). Both processes provides essentially the same type of information such as the energies of molecular vibrational modes since they detects molecular vibrations. However, they differ by their selection rules and fundamental mechanisms. For example, an electrically unsymmetric bond may be IR active and Raman inactive or both IR and Raman active [4]. An important withdraw of IR method is that aqueous system such as live plants cannot be use IR method because water is very strong absorbent of IR, whereas Raman

3
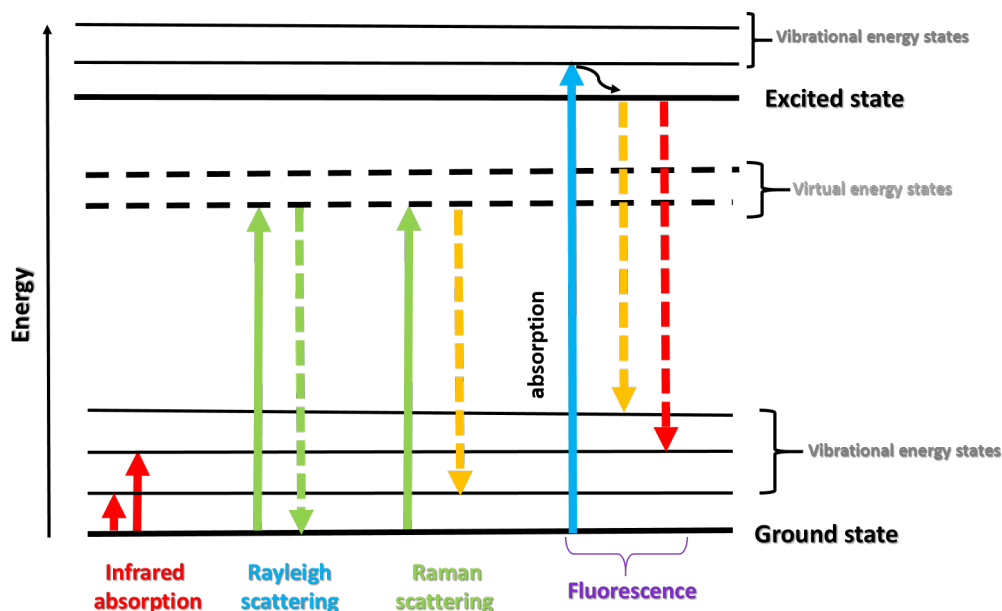
Figure 1.2: The energy level diagram of Infrared, Fluorescence, Rayleigh, and Raman processes

process doesn't affect much with water. Overall, both methods have advantages and limitations, but can be used as complimentary methods for example studies on bond angles, bond lengths, and other structural information require Raman data in addition to IR analysis [5].

Raman Spectroscopy: Its Instruments and Applications

Raman spectroscopy is a technique specialized to measure frequency shift of inelastic scattered light (Raman process) from a sample when incident light hits a molecule of the sample and produces scattered light [2]. It should be obvious from Figure 1.1B that Raman frequencies will appear $\pm\nu_v$ (a molecular vibration frequency of sample)relative to that excitation frequency at ν_0. Generally, a vibrational frequency has value of the order of $10^{12}s^{-1}$. A Raman shift expressed by a wavenumber

4

in units of cm^{-1}, which is defined by

$$\overline{\nu}_v = \frac{\nu_v}{c} = \frac{1}{\lambda_v} \qquad (1.1)$$

where λ_v is a the corresponding wavelength and c is the velocity of light. This frequency shift depends upon the chemical composition of the sample (molecules) which are responsible for the Raman scattering. Therefore, Raman measurements provide important information of molecular characterization of sample [9]. The intensity of Raman scattering linearly depends on the total amount of sample's molecular polarization changes. Raman technique doesn't need any sample preparation and non invasive method, but it is a very weak process. The intensity of the Rayleigh scattering three orders (10^{-3}) and the intensity of the Raman scattering 6 orders (10^{-6}) weaker than the incident light intensity. Until the last decade, Raman spectroscopy has not been as widely applied because of low efficiency of Raman scattering and detection instruments were expensive and bulky. However, many of these problems have been overcome and even portable field instruments are now available. In the section 3, we used a handheld Raman equipment for collecting Raman spectra from cow feces and forages. The figure 1.3 shows a typical setup of Raman spectrometer. Excitation light from a laser reflected from a sample and the Rayleigh scattered light (from sample) will be rejected by a notch filter (Raman filter) which allows only Raman scattered light to pass. Raman scattered light from sample will collected by collection optics and send to a spectrograph which consists of a grating and a charge-coupled array detector(CCD)(see Figure 1.3). Many advances in Raman instrument design implemented such as highly sensitive detectors, spectrometers, Rayleigh rejection filters (Raman filters), sources (excitation lasers) and collection optics (better lenses, objective etc). These advances have shortened analysis time

5
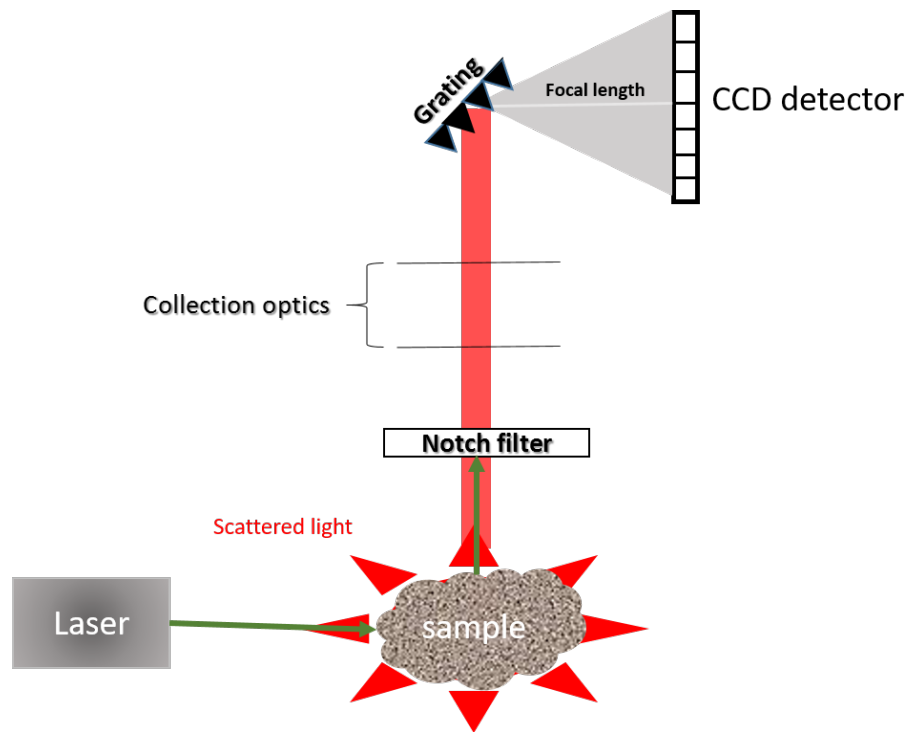
Figure 1.3: A simple setup of a Raman spectrometer.

which used to collect Raman signal from a sample and increased Raman signal-to noise ratios(much clean Raman spectra). One of the advances was a development of Raman microscopy [6]. It uses a microscope objective instead a lens which allows excitation light to focus more on a sample and collects Raman light in a wider angle than a lens. Further advances such as a confocal Raman microscopy developed in early 1970s [7] . The Figure 1.4 shows a simple schematic of a confocal microscope. Unlike a Raman microscope, where Raman signal collected from an entire field of excitation, the confocal system measures at any one time the intensity of Raman signal from a very small area of sample. It yields significant improvements in both the contrast and spatial resolution of Raman signal of sample and allows to do a depth profiling of a sample. In other words, it allows an optical sectioning of sample without cutting or physical dissection. Many researches have used confocal Raman
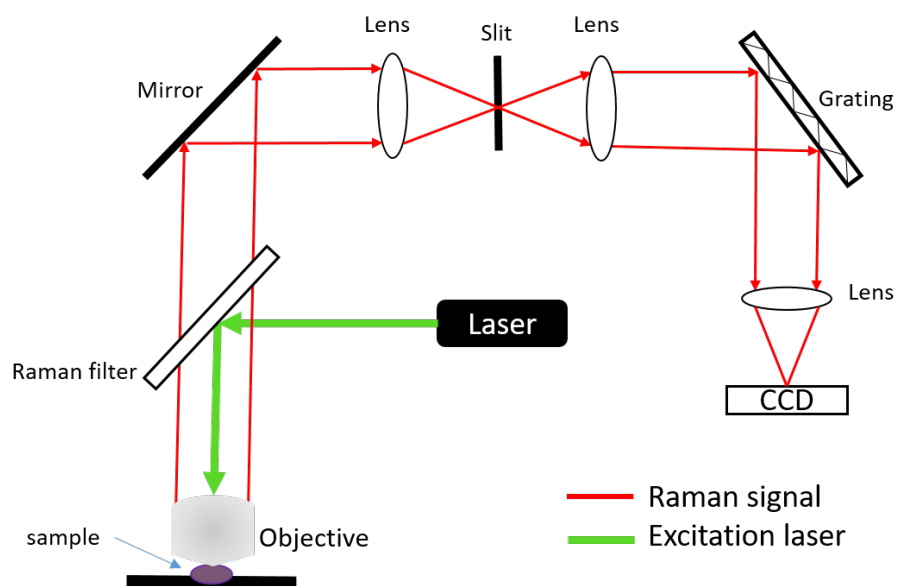
Figure 1.4: Schematic diagram of a confocal Raman microscope.

microscope to study two (2D) and/or three dimension (3D) molecular composition of layered systems such as biological tissues, plant cells, polymer etc [8, 9, 10, 11]. In the section 2, we studied plant abiotic stress responses via a confocal Raman microscope.

IN VIVO DIAGNOSTICS OF EARLY ABIOTIC PLANT STRESS RESPONSE VIA RAMAN SPECTROSCOPY*

In this section, Raman spectroscopy was utilized to nondestructively detect abiotic stress responses of plants. Development of a phenotyping platform capable of non-invasive biochemical sensing could offer researchers, breeders, and producers a tool for precise response detection. In particular, the ability to measure plant stress in vivo responses is becoming increasingly important. In this work, a Raman spectroscopic technique is developed for high-throughput stress phenotyping of plants. We demonstrate for the first time, the early (within 48 hours) in vivo detection of plant stress responses. Coleus (*Plectranthus scutellarioides*) plants were subjected to four common abiotic stress conditions, individually: high soil salinity, drought, chilling exposure, and light saturation. Plants were examined post stress induction in vivo where changes in the concentration levels of the reactive oxygen scavenging pigments were observed by Raman microscopic and remote spectroscopic systems. The molecular concentration changes were further validated by commonly accepted chemical extraction (destructive) methods. Raman spectroscopy also allows simultaneous interrogation of various pigments in plants. For example we found a unique negative correlation in concentration levels of anthocyanins and carotenoids which clearly indicates that plant stress response is fine-tuned to protect against stress-induced damages.This precision spectroscopic technique holds promise for the future development of high throughput screening for plant phenotyping and for the quantification of biologically or commercially relevant molecules such as antioxidants and

pigments.

Introduction

With the global population projected to exceed 9 billion by the year 2050 the task of producing enough food and energy for the world is of utmost importance [12]. In anticipation of rising food demand[13], the ability to measure plant stress *in vivo* is becoming increasingly vital for increasing agricultural production and research. For example, such technologies would allow a farmer to intervene upon stress detection and also makes practical the development of crop varieties with increased tolerance to abiotic stress. The field environment requires a comprehensive and rapid screening technology for plant physiological, biochemical and morphological characteristics [14]. Such characteristics can be integrated to predict plant growth potential, biomass processibility, and abiotic stress responses before any visible signs occur in a plant. Plant growth is impacted by unseasonable droughts, cold, increased UV radiation and high-energy blue light associated with atmospheric changes in ozone levels, and fertilizer/irrigation application associated with increased soil salinity [15, 16]. Most existing methods for evaluating biochemical characteristics use destructive chemical analysis which require time and intensive labor. In addition, these methods use strong chemicals which require special handling and disposal. Currently *in vivo* sensing technologies are limited by the time required for detecting a stress response, types of stress factors which can be detected, the level of stress, and/or physiological changes. For example, reflectance spectroscopy [17], chlorophyll fluorescence spectroscopy [18],infrared thermal imaging [19], terahertz time domain spectroscopy [20], and hyperspectral imaging [21] techniques have all been used to measure stress indirectly by focusing either on changes in chlorophyll ratios/contents [17, 18], physical changes [20] or water status of plants [19, 21]. Surprisingly, Raman

spectroscopy has not been very widely used. Raman spectroscopy has been used for nondestructive and biochemically specific detection of trace molecules for applications such as cancer and pathogen detection, agriculture applications and other plant studies such as imaging of the plant cell wall [22, 23, 24, 25, 11]. Near infrared spectroscopy provides a complementary methodology to Raman spectroscopy, however it has water absorption limitations. The Raman spectroscopic technique, on the other hand, is a valuable *in vivo* tool which deals with highly complex samples in their environment and is relatively insensitive to water. An important advantage of Raman spectroscopy is the ability to interrogate multiple molecular species simultaneously. For the purposes of identifying abiotic stress response *in vivo* in plants, we address, for the first time, a novel comparison between molecule biosynthesis and degradation associated with elicited general abiotic stress through utilization of Raman spectroscopy. In this study, two molecules anthocyanins and carotenoids were observed across all four abiotic stress factors (see, Figure 2.1). When plants are exposed to abiotic stresses, they undergo highly complex physiological, biochemical, and molecular changes [15, 16, 26]. In particular, reactive oxygen species (ROS) accumulate in plants during abiotic stresses which are highly reactive and toxic and the plant tries to eliminate them by producing volatile derivatives and antioxidants [27]. Carotenoids which are one of the target molecules in this study are considered to be the first line of defense against ROS, serving as the main $^1O_2$ quencher in chloroplasts [28, 29, 30, 31]. The oxidative degradation of accessory photosynthetic pigments like β-carotene and other carotenoids leads to the accumulation of different volatile derivatives such as β-cyclocitral that has been shown to serve as a molecular signal responsible for induction of $^1O_2$ responsive genes [28, 29]. Therefore, rapid conversion of β-carotene to β-cyclocitral during oxidative stress is suggested to be one of the major defense mechanisms against ROS [28, 29]. The second tar-
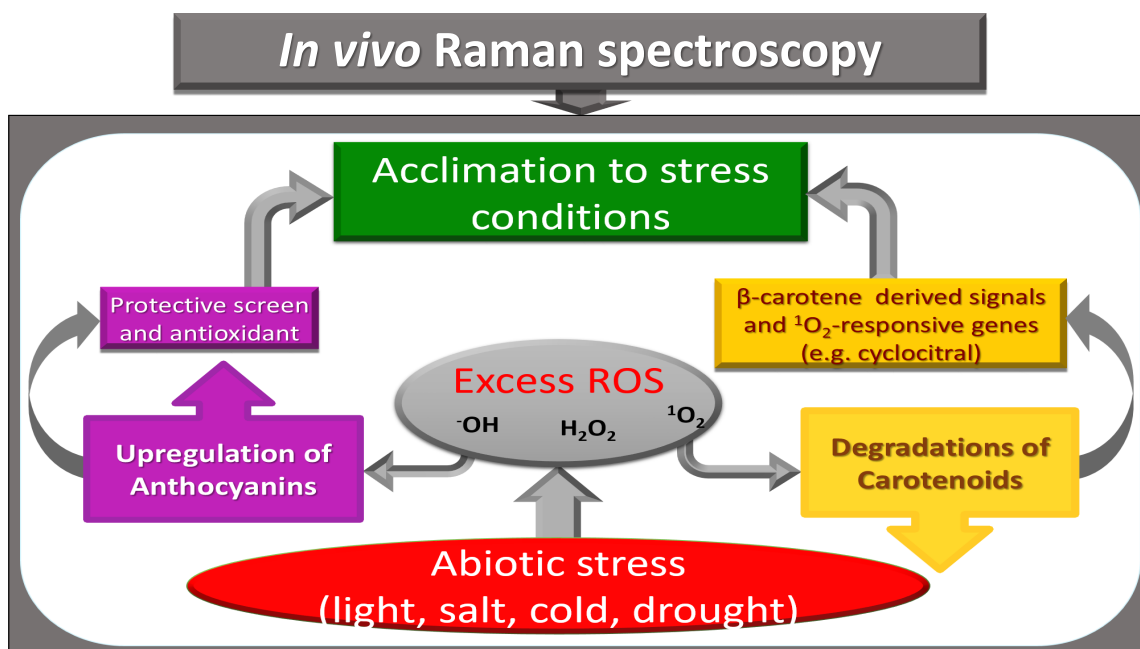
Figure 2.1: A simultaneous and *in vivo* detection of anthocyanins and carotenoids which are reactive oxygen scavenging pigments by the Raman technique.

get molecule, anthocyanin, a water-soluble pigment derived from flavonoids has long been associated with plant stress response [26, 32, 33]. Anthocyanin protection is two-fold: first as an osmotic regulator, and second as a light filtering and free radical scavenging protective pigment [26]. Anthocyanins, which exist almost exclusively as glycosides, can be transported via a plant's vasculature along with other solutes, and eventually accumulate in the cell's vacuoles. This osmotic regulation through solute concentration protects plants from the damaging effects of various abiotic stresses [26, 32, 33, 34, 35]. As photo filters, anthocyanins block damaging intense blue, UVA, and possibly UVB light for the leaf, lowering the light absorption burden for the photosynthetic molecules. In this work, Raman spectroscopy is utilized for high-throughput stress phenotyping and early stress detection *in vivo* with improved sensitivity and the ability to interrogate individual molecules such as carotenoids

and anthocyanins simultaneously.

Materials and Methods

Plant Preparation and Treatment

Coleus lime (*Plectranthus scutellarioides*) plants were used as an experimental model [33, 36]. The seeds were obtained from a commercial source (Outsidepride.com). The experiments were carried out in the lab with automatic environmental controls (Institute for Quantum Science and Engineering, Texas A & M University). The seeds were initially grown under T5 grow lights on a 16/8 hour light-dark cycle for 11 weeks. Next, cuttings were taken from a single fully grown plant to further multiply into cloned plants as it provided that the plant responses to stress were not due to genetic discriminations or mutations. These cloned plants were grown under the same conditions mentioned above for 71 days. The experimental model plants were subjected to one of the four environmental stresses: salinity, drought, chilling temperature, or excess light. All plants received a nutrient solution every two weeks. For saline stress, the plants were irrigated with 200 mM NaCl solution (pH=7) at day 1 and day 3 , alternately with distilled water (pH=7), whereas, for drought stress, normal watering was withheld. For cold stress, the plants were kept at chilling temperatures (4^0C) for 8 hours during their dark period on day 1 and day 2. Finally, for light stress, the plants were exposed to an intense light source (flood light with 100 W high pressure sodium light bulb) for 3-4 hours (in addition to the T5 grow light) day 1 and day 3. The temperature and humidity levels were fairly stable (72F, and 47% of humidity). Soil pH levels of the plants were constantly monitored. Each treatment had 10 replicate plants, eight were harvested for chemical analysis and two were used for spectroscopic measurements. Plants used for chemical analysis were harvested at 12 hour intervals. Spectroscopic measure-

ments via Raman allow us to use a single plant without destroying it, so we used two plants for statistical purposes. Pure chemicals including beta carotenoid, lycopen, xanthophyll, anthocyanins (pelargonin chloride, peonidin 3-o-glucoside chloride, callistephin chloride, delphinidin chloride, malividin chloride, keracyanin chloride) were obtained from Sigma-Aldrich.

Spectroscopic Measurements and Data Processing

A Raman confocal microscopic system equipped with a 532 nm CW laser was used for the microscopic measurements (Horiba, LabRam HR Revolution). Its simplified setup is in Figure 2.2A. The remote Raman spectroscopic measurements were performed using a custom built spectroscopic system that is easy to transport to a field. It is considered to be a remote sensing system because it detects a signal at a 10 cm distance (see Figure 2.2B). The laser source at range system was a 532 nm CW laser and the sampling spot size was 200 μm. Plant leaves were placed directly on the sample holder without physical detachment from the plant. Therefore it is considered as *in vivo*, non-destructive detection. The laser induced scattered radiation (signal) were efficiently detected by air cooled CCD cameras. The laser powers were adjusted for the plant tissues without affecting the live cells. (0.5 mW with 1 second acquisition time and 10 mW with 10 second acquisition time respectively for microscopic and spectroscopic measurements). 20 Raman spectra were collected from four leaves of each plant. These four leaves were selected from different locations of the canopy of the plant. The Raman spectral data of the plants (leaves) were obtained every 12 hours during the on-set and development of stress until 72 hours. Since the leaves are a complex system, we used the mean spectra for further analysis. The greater contributor of the noise to Raman spectra are the intrinsic fluorescence of molecules in plant tissues. Therefore, in order to extract Raman signal from the raw spectrum
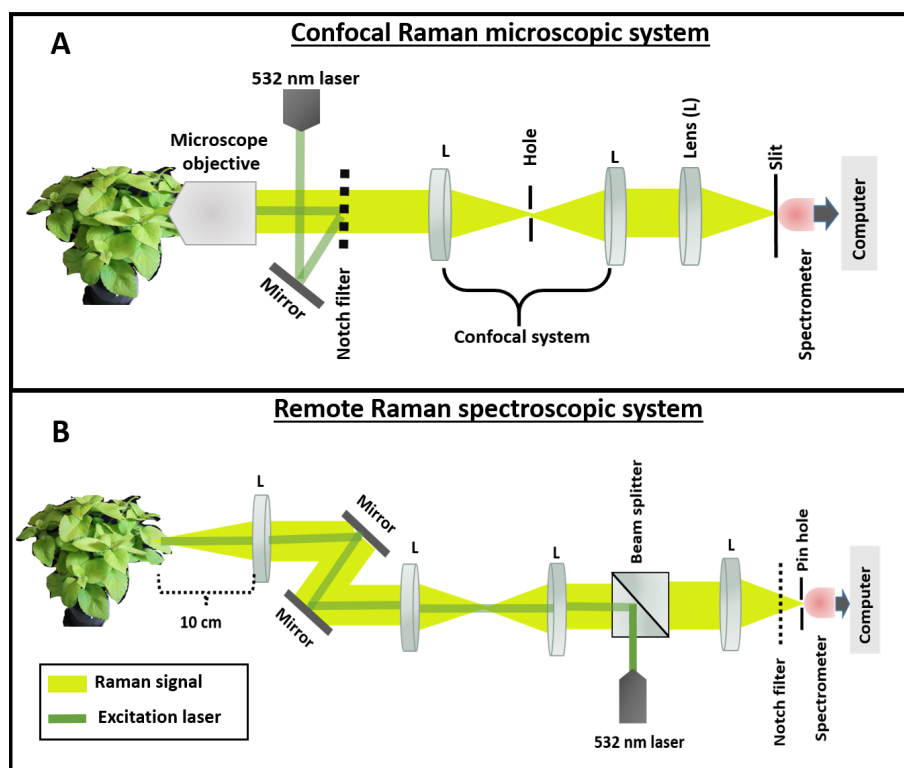
Figure 2.2: The Raman system setups A) Confocal Raman microscopic system, B) The remote Raman spectroscopic system.

acquired, it is necessary to remove the fluorescence background. The baselines of Raman raw spectral data were corrected by fitting the high order polynomials with multiple iterations [37]. The spectra were further smoothed by the Savitzky-Golay algorithm with 15 adjacent points. All data processing programs were written in MATLAB R2013a (The Mathworks, Natick, MA, USA).

Chemical Extraction and Analysis

Immediately following spectral data collections, leaves from the replicate plants were sampled for chemical destructive analysis. Square cut leaf parts from each plant were immediately stored in liquid nitrogen, then in a minus 80^oC-freezer. From those frozen samples, eight were used for total carotenoids and five were used for total an-

thocyanins extraction for each plant. The plant tissues were extracted by the method of Lightenthaler et al. [38] with 100% acetone. The extracted solution's absorbance was read at 470, 645, 662, and 750 nm with a Thermo Scientific GENYSIS 10S UV-VIS spectrophotometer. Total carotenoids were calculated using the equations given in [39]. Anthocyanins were extracted by using an acidified methanol. One μl of a 50% methanol, 3% formic acid and 47% distilled water solution were added to each 50 μg of the plant tissues and used the protocol of [32] The extracted solutions were passed through 0.4 μm filter and the absorbance read at 532 nm by the above spectrophotometer as in [32].

Main Results and Discussions

Raman Spectroscopic Detection

Photosynthetic pigments - anthocyanins and carotenoids, are found naturally in plant tissues. Moreover, anthocyanin biosynthesis is often induced in the leaf's upper epidermis by excess light irradiation, cold, drought and saline stresses. Understanding their biosynthesis is, in fact, at the heart of the plant stress tolerance mechanism justification [26, 34, 35]. By targeting anthocyanins and carotenoids for the purposes of identifying abiotic stress responses in plants, we utilized a Raman spectroscopic technique. To implement Raman spectroscopy a laser light is used to excite molecules. The molecules emit light with a new optical frequency that is downshifted from the incident laser frequency by the amount equal to their vibrational frequencies. This new color (referred to as Stokes radiation) is further detected with a spectrometer. The Raman spectra of the plants were recorded for 48 hours post induction for all four types of stresses (saline, excess light, drought and cold) including spectra of the unstressed control plants by using both a commercial Raman confocal microscope and a lab-built (portable) remote Raman system (see Fig.

15

2). The Raman microscopic spectra at 48 hours post-stress are compared to the unstressed control plants in Figure 2.3. Carotenoids were distinguished in the spectra
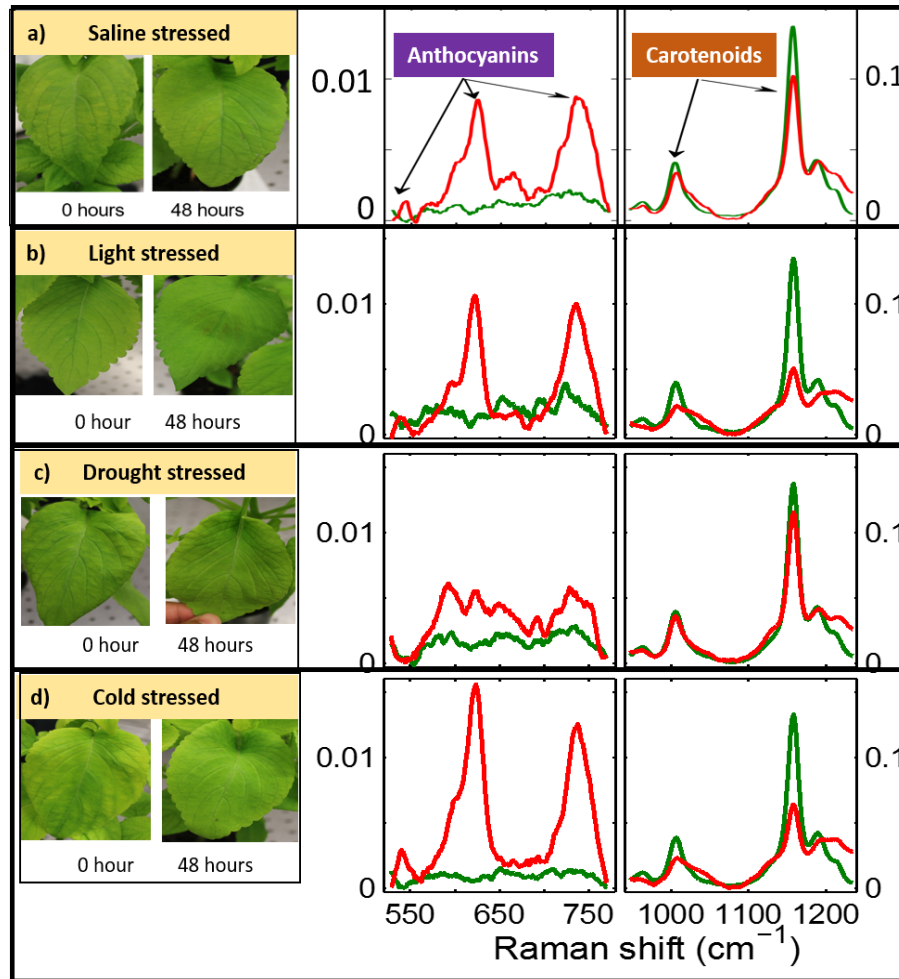
Figure 2.3: The Raman spectra of unstressed plants (green curves) and stressed plants at 48 hours post-stresses (red curves) of a) saline, b) light, c) drought, and d) cold. Inset: Photos of coleus leaves for unstressed (left) and stressed (right) plants.

for the control plants with distinct narrow peaks at 1007 and 1157 cm^{-1} [40, 41]. After abiotic stress exposure, the Raman peaks at 539, 623 and 733 cm^{-1} for anthocyanins [42, 43, 44] clearly stood out. The set of Raman spectra of the plants

were recorded initially (0 hour) and every 12 hours for up to 72 hours induction for all four types of stresses. The explicit height of the Raman peaks changes indicating the concentration of two pigments varies over time. Quantitative estimations of relative concentration variations of the pigments in plant tissues under stress can be derived from the recorded Raman spectra by using our newly developed least squares regression fitting method. For the sake of simplicity, although without losing most valuable information, we constructed a fitting as a linear combination of the recorded Raman spectra of only two pure chemicals: pelargonin chloride [32, 44] and β-carotene [40, 41]. A similar least squares method has been developed [22, 45] for successful diagnostics of breast cancer. The obtained fit coefficients represent relative change in the concentration of the base pigments with certain offset. In fact, these fit coefficients are functions of both the concentration of particular chemicals and their Raman scattering cross-sections. Moreover, due to the fact that the plant tissue is heterogeneous, the fitting coefficients are separately normalized. This allows the relative change to be quantified. We obtained the relative changes in carotenoids (brown bars) and anthocyanin (violet bars) as functions of duration of stress (see Figure 2.4). The carotenoids decreased while anthocyanins increased the longer the plants were stressed. In the control plants carotenoids and anthocyanins levels were not altered. We note that the Raman spectra of carotenoids [40, 41] and anthocyanins molecules [42] in live plants have been previously studied one at a time. In this work, to our knowledge for the first time, we directly measured the changes in molecule concentrations of anthocyanin and carotenoid molecules simultaneously. From the plant physiological view point, negative correlation between anthocyanins and carotenoids can be understood as follows. Considering that both of the pigments are involved in response to reactive oxygen species, this negative correlation highlights the effectiveness of the intracellular regulation. Under stress conditions,

17
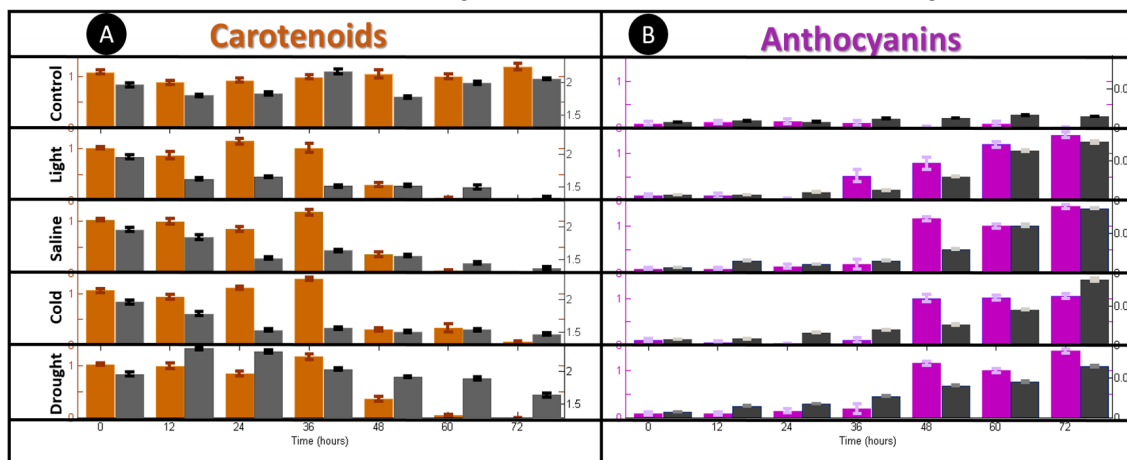
Figure 2.4: (A) The bar distributions for the fit coefficients for carotenoids (brown), chemically extracted value for carotenoids (mg/g dry weight)(grey) as functions of durations of the abiotic stresses; (B) The bar distributions for the fit coefficients for anthocyanins (violet), chemically extracted value for anthocyanins (μg/μl dry weight)(black) as functions of durations of the abiotic stresses.

the strong induction of ROS [28, 29, 30, 31] and the down-regulation of photosynthetic activity leads to the degradation of carotenoids. Recent research has shown that β-carotene is rapidly converted to a novel volatile molecular signal β-cyclocitral, which regulates expression of a set of $^1O_2$ responsive genes in plants. Therefore, it is plausible that the observed reduction of β-carotene in this study can be explained by its rapid conversion to β-cyclocitral. While carotenoids degrade, anthocyanins accumulate as a stress responding ROS scavenger[26, 32, 33, 34, 35]. The strong negative correlation between the two pigments indicated that signal transduction has fine-tuned the transcriptomic, proteomic and metabolic process to allow the cell to properly adjust to stress conditions.

A Remote Raman Spectroscopic Detection of Carotenoids in Plant

We built a portable at range Raman spectroscopic system. The recorded Raman spectral relative changes in carotenoids via a portable Raman spectroscopic platform were consistent with the Raman microscopic data thereby demonstrating the capacity of Raman spectroscopy for real life *in vivo* monitoring of stress responses of crops in the field (Figure 2.5). However, it must be noted that our remote system was
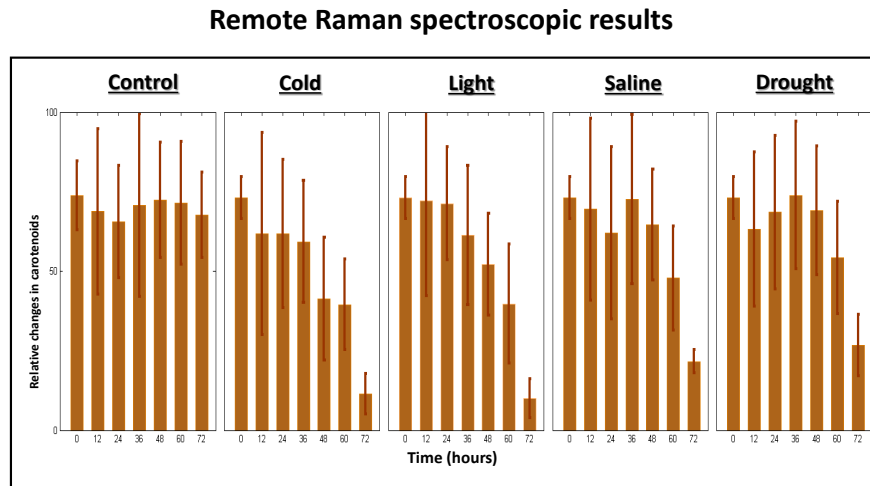
Figure 2.5: The bar distributions for carotenoid relative changes measured by the remote system as functions of durations of the abiotic stresses.

not sensitive enough to measure anthocyanins. Further improvements for our system will be to increase the collection efficiency, to reduce background fluorescence, and to implement high sensitivity detectors.

Comparison of the Raman Technique with Existing in Vivo Plant Stress Sensing
Techniques

The Raman technique demonstrates distinct advantages over established in vivo plant stress sensing techniques such as reflectance spectroscopy [17], chlorophyll fluorescence spectroscopy [18],infrared thermal imaging [19], terahertz time domain spectroscopy [20],and hyperspectral imaging [21]. It offers earlier detection, biochemical selectivity, the ability to detect multiple stress conditions, and the detection of initial defense responses. The Raman technique is capable of detecting changes in carotenoids and anthocyanins which are one of the first line defense responses of plants during abiotic stress. The existing sensing techniques detect changes in chlorophyll, water status, or physical appearance which are consequences of abiotic stress. Raman directly detects plant stress responses within 2 days for four different stress conditions. The terahertz time domain spectroscopy [20] which had been considered the fastest existing technique has indirect detection, is only capable of detecting drought stress and takes 3 days.

Validations via Chemical Analytical Extractions

Finally, we performed the traditional chemical analytical extractions. This is however, a destructive method, only one pigment's concentration can be extracted at a time. We collected plant tissues after each Raman spectroscopic measurement. We used the chemical extraction protocols of anthocyanins as in [32] and carotenoids as in [38]. Fig. 4 shows the absolute values of the total carotenoids (grey bars) and anthocyanins (black bars) over time for all treatments. The changes in total carotenoids and anthocyanins from the chemical analysis show strong agreement with the Raman spectroscopic data for all applied stress conditions. It, thus, validates the Raman technique as an appropriate sensor for these pigments.

20

Conclusions

We demonstrated, for the first time, early detection of plant stress responses using *in vivo* Raman spectroscopic methods with improved sensitivity and the ability to interrogate individual stress-indicator pigment molecules simultaneously. The variations in the concentration levels of anthocyanins and photosynthetic carotenoids in coleus plants were observed across abiotic stresses including high salinity, drought, cold, and excess light. These changes over time post-stress induction provides Raman spectroscopy as a method of accurate measurement of these molecules, while indicative of the functional relationship of these pigments in response to excessive ROS during abiotic stress. This work furthers our understanding of plant physiology by detecting a novel negative correlation in the levels of anthocyanins and carotenoids during the stress response. The short term response across multiple abiotic stresses holds promise for a near ubiquitous method of abiotic stress detection. Finally, our proposed portable system has the capability to become mobile and automated to allow for increased utility in precision agricultural applications both for breeders and commercial producers. The traditional chemical analytical extraction also validated the existence of the concentration changes either, in total anthocyanins or carotenoids. In general, the Raman technique could be a cheap, rapid, non-destructive, and alternative to chemical analysis. Since it is *in vivo*, it detects changes of these molecules over time from one plant which is impossible in destructive chemical analysis.

COMPARISON OF NIRS AND RAMAN SPECTROSCOPY FOR PREDICTING BOTANICAL COMPOSITION OF CATTLE DIETS*

In this section, we utilized Raman spectroscopy to predict cow diets by their feces. Diet selection is an important driver or ecosystem structure and function that is difficult to measure. Because of advances in spectroscopy new instruments are available for evaluating their applicability to ecological field studies. The objective of this study was to compare near infrared spectroscopy (NIRS) to Raman spectroscopy of fecal samples for predicting the percentage of Honey mesquite *Prosopis glandulosa Torr.* in the diet of ruminally fistulated cattle fed three different base hay diets and to compare them for their ability to discriminate among the three base diets. Spectra were collected from fecal materials from a feeding trial with mesquite fed at 0, 1, 3 and 5% of the diet and base hay diets of timothy hay *Phleum pratense L.*, Sudan hay *Sorghum sudanense (Piper) Stapf*, or a 50 : 50 combination of Bermuda grass hay *Cynodon dactylon (L.) Pers.* and beardless wheat hay *Triticum aestivum L.* NIRS and Raman spectra were used for partial least squares regression calibrations with the timothy and Sudan hays and validated with the Bermuda grass beardless wheat hay diets. NIRS spectra provided useful calibrations (R^2=0.88, slope=1.03, intercept=1.88, root mean square error=2.09, bias=1.95, ratio of performance to deviation=2.6), but Raman spectra did not. Stepwise discriminant analysis was used to select wavenumbers for discriminant among the three hays. Fifteen of 350 possible wavenumbers for NIRS spectra and 29 of 300 possible wavenumbers for Raman spectra met the $P \leq 0.05$ entry and staying criteria. Canonical discriminant analysis

using these wavenumber resulted in 100% correct classification for all three base diets and the Raman spectra provided greater separation than NIRS spectra. Discrimination using Raman spectra was primarily associated with wavenumbers associated with undigestible constituents of the diet, i.e., lignin. In contrast, discrimination using f.NIRS spectra was primarily associated with wavenumbers associated with digestible constituents in the diet, i.e., protein, starch and lipid. We believe that Raman spectroscopy deserves further investigation as a quantitative technique in ecological field studies.

Introduction

Honey mesquite *Prosopis glandulosa Torr.* is an invasive shrub that is common in the southwestern US and northern Mexico. The leaves of honey mesquite have forage quality characteristics similar to moderate quality hay, with crude protein levels of 12 to 20% and neutral detergent fiber levels of 35 to 40% [49, 58] Mesquite leaves are available during late spring and early summer before monsoon rains when grasses are typically dormant and low quality. However, mesquite leaves contain secondary compounds, including alkaloids and phenolic compounds [46, 72] which limit intake by livestock. Animals that can consume small amounts of mesquite may be more adapted to southwestern rangelands than animals that avoid mesquite. Development of a method to cost effectively determine the amount of mesquite in cattle diets would facilitate selection of animals more adapted for rangelands in the southwestern US. Near infrared reflectance (NIRS) spectroscopy has a long history as a spectroscopic technique with useful applications in agriculture [71] and ecology [53]. In contrast, Raman spectroscopy has not been as widely applied because of early difficulties with sample degradation and fluorescence; however, many of these problems have been overcome [25] and portable field instruments are now available. NIR

spectra originate from absorption of light by vibrating and rotating molecules and Raman spectra originate from scattering of light by vibrating and rotating molecules. NIRS detects vibrations when the electrical dipole moment changes, while Raman spectroscopy identifies vibrations caused by electrical polarizability changes. NIR spectra are characterized by broad, often overlapping peaks that are matrix dependent and affected by moisture content. In contrast, Raman spectra have narrow, highly resolved peaks that are not affected by matrix or moisture. Another advantage is that mononuclear diatomic molecules (O_2, N_2 etc.) are Raman active, but do not absorb in the NIR Range. However, an electrically unsymmetric bond may be NIR active and Raman inactive or both IR and Raman active [47, 51]. Disadvantages of Raman are weak signal to noise ratio, sample heating, and sample fluorescence. Because Raman is a weak process, it requires high power and high sample purity. Consequently Raman is most commonly used for homogenous samples and NIRS is often used for heterogeneous samples. Both methods have advantages and limitations, but can be used as complimentary methods for example studies on bond angles, bond lengths, and other structural information require Raman data in addition to NIR analysis[5]. Previous studies using diet fecal pairs and NIRS (f.NIRS) to predict diet composition have used dried and ground feces [67, 68]. Because Raman spectroscopy has the potential to be effective without processing of feces and potable instruments are available, the objective of this study was to compare f.NIRS to Raman for predicting the percentage of mesquite in cow feces and the discrimination of base diets by the two techniques.

Methods

Feeding Trial

This research was conducted at New Mexico State University Campus Livestock, Education, and Research Center (Las Cruces, NM) during November and December 2013. Fecal material was obtained from a feeding trial where known amounts of honey mesquite leaves were introduced intraruminally into six ruminally fistulated cows. Cows were mature Hereford x Angus crosses with an average weight of 568 kg. Honey mesquite leaves were harvested from the Chihuahuan Desert Rangeland Research Center located 35 km north of Las Cruces, NM during July 2013. Leaves were harvested by hand and allowed to air dry. During a 14 d pretrial period, animals were fed beardless wheat hay *Triticum aestivum L. ad libitum.* Following the pretrial, 2 animals were randomly assigned to one of three base diets, namely: timothy hay *Phleum pratense L.* a C3 perennial, Sudan hay *Sorghum sudanense (Piper) Stapf* a C4 annual, or a 50 : 50 combination of Bermudagrass hay *Cynodon dactylon (L.) Pers.* a C4 perennial and beardless wheat hay a C3 annual (BW). Base rations (hay) were fed, and refusals were collected and weighted daily. The base hay rations were fed for four periods of increasing levels of mesquite. The initial period was 9 day when no mesquite was fed and base ration was fed at 2% of body weight. The subsequent periods were 7 day each. For the second period, the base ration was fed at 1.9% of body weight and 1% of the diet was mesquite leaves. For the third period, the base ration was fed at 1.7% of body weight and 3% of the diet was mesquite leaves. For the fourth period, the base ration was fed at 1.5% of body weight and 5% of the diet was mesquite leaves. Each morning at approximately 800 hr during the final 3 periods, air dried mesquite leaves that were ground to an approximate length of 1 cm were introduced through a rumen cannula. Fecal samples were collected at

the same time on the final 2 days of each period. Previous research (Walker et al. 2010) showed that NIR determined percentage juniper in the diet of goats did not change after the third day when percentage juniper in the goat diet increased from 0 to 10%. Mesquite leaves and the base rations were analyzed for DM, ADF, NDF and crude protein by SDK Laboratories (Hutchison, KS). Dry Matter was determined by oven drying for 3 hr at 105Â°C ADF (NFTA Method 2.1.4). Acid detergent fiber (ADF) and neutral detergent fiber (NDF) analysis was completed using the filter-bag technique (ANKOM filter bag technique; ANKOM Technology Corp, Fairport, NY). Crude protein was determined by Kjeldahl N (AOAC Method 976.06) multiplied by 6.25.

Spectra Acquisition

All samples were dried at 60^0C and ground in a Wiley mill to pass a 1 mm screen, and then ground a second time in a Wiley mill to pass a 0.5 mm screen., For f.NIRS analysis, daily fecal samples for each animal were packed into sample cells with a near-infrared transparent quartz cover glass, and scanned 32 times using a NIR Systems, Inc. (Silver Spring, Md.) model 6500, scanning reflectance monochromator. Reflected energy ($\log \frac{1}{R}$) was measured, averaged over the 32 scans and recorded at 2- nm intervals from 400 to 2,500 nm (wavenumbers 4000-25000 cm^{-1}). A personal computer, interfaced to the monochromator, used ISI NIRS2 version 3 software (Infrasoft International, Port Matilda, Penn.) to collect spectra. Raman spectra of the ground samples were acquired with a Rikagu handheld Raman analyzer with 1064 nm continuous wave laser. The spectra were collected in the wavenumber range of 200-2000 cm^{-1}. Feces were placed in a sample vial supplied with the instrument and each sample was scanned 8 times by rotating the vial 45^0 between each scan. Each scan consisted of the average of 5 spectra collected during a 2 second acquisition

time. Data from the eight scans were averaged for analysis.

Data Analysis

Daily hay intake (g/kg BW) was analyzed for the fixed effect of hay with percentage mesquite and day as repeated measures using PROC GLM (SAS, 2004). The Unscrambler 9.7 (Camo SoftwareAS, Oslo, Norway) was used to perform pretreatment and partial least squares (PLS) regression [54]. For the f.NIRS analysis, number of spectra were reduced by averaging 3 adjacent wavelengths, smoothed with a three segment moving average, and finally a second derivative was calculated using the Savitzky-Golay method [60] using a second order polynomial and a five segment gap. The transformed data was mean centered and PLS regression was conducted with cross validation using a random leave out of 12% of the observations. The Raman spectra was transformed by applying a baseline correction using detrend with a third order polynomial, standard normal deviate, and a Savitzky-Golay first order polynomial 31 point smooth. The transformed data were not mean centered and partial least squares regression was conducted with cross validation described previously. Validation of was performed for f.NIRS and Raman spectra using spectra from the Sudan and Timothy based diets for calibration and predicting the Bermuda bearded beardless wheat hay diets for validation. Discriminant analysis (SAS 2004) was used to determine if the untransformed spectra could be used to classify the three hays used in the base diets. To avoid singular matrices that were caused by high multicollinearity of the spectra, stepwise discriminant analysis (PROC STEPDISC) with probability of entry and staying set at $P \leq 0.05$ was used to select the wavenumbers for canonical discriminant analysis. Data were divided into calibration and test sets and canonical discriminant analysis (PROC DISCRIM) was used to determine if the hays could be correctly classified. Four test set classifications were performed using

a leave out one level of mesquite whereby all samples at 3 levels of mesquite were used for development of the discriminant function to classify the samples in the left out levels. Thus, four test and calibration sets were evaluated.

Results

Honey mesquite leaves had a higher crude protein concentration than the hays (Table 3.1). Mesquite leaves also contained less neutral detergent fiber (NDF)

Table 3.1: Dry matter (DM), crude protein, neutral detergent fiber (NDF) and acid detergent fiber (ADF) of the honey mesquite leaves, beardless wheat hay, Bermuda grass hay, Sudan grass hay and timothy hay expressed on a DM basis.

Diet Item	DM, %	Crude protein,%	NDF,%	ADF, %
Honey mesquite leaves	96.27	16.39	40.10	33.21
Bermuda grass Beardless wheat hay	95.93	7.75	62.66	42.53
Sudan grass hay	95.23	5.19	58.86	41.29
Timothy hay	95.31	12.02	57.18	36.46

and acid detergent fiber (ADF). The dry matter content of the mesquite leaves was slightly higher than the hay rations. Timothy was the highest quality hay followed by BW. Sudan was the lowest quality hay and the CP level of this hay was below the maintenance requirement of beef cattle (2000 NRC) and the requirement of ruminant bacteria [65].). Intake did not differ between hays (P>0.47), day (P>0.11), or their interaction (P>0.78). There was an effect of percentage mesquite (P<0.01) and the mesquite by day interaction (P<0.02) Figure 3.1. Calibration, cross validation and validation results are shown for predicting percentage mesquite in the diets in Table 3.2 . f.NIRS spectra provided useful calibrations but Raman spectra did not. f.NIRS cross validation indicated the optimal number of factors in the model
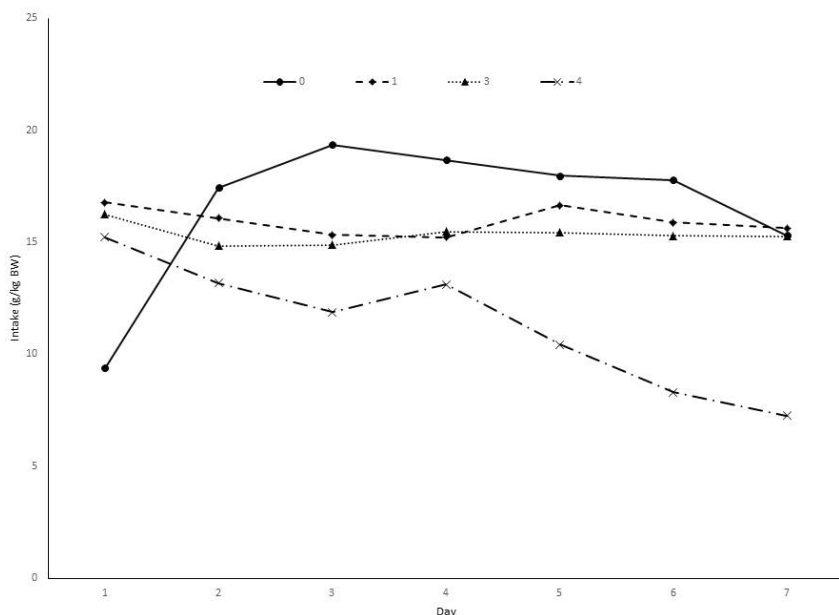
Figure 3.1: Hay intake (g/kg BW) averaged across three different hays as affected by juniper as a percentage of total intake placed in the rumen.

was three. However, validation results showed that a five factor model gave the best results. Precision improved for validation compared to cross validation (R^2 = 0.70 and 0.88, respectively). Increasing factors in the cross validation model to more than three decreased the simple coefficient of determination (R^2). The slope of the validation data (1.03) was also improved compared to the cross validation data (0.73). Statistics that measure accuracy, RMSE and bias, were greater for the validation data (2.09 and 1.95, respectively) than for the cross validation data (1.11 and 0.01, respectively). The ratio of performance to deviation (RPD) was 1.8 and 2.6 for cross validation and validation, respectively. Raman and f.NIRS spectra on which the stepwise discriminant analysis was performed are shown in Figure 3.2.

Fifteen of 350 possible wavenumbers for f.NIRS spectra and 29 of 300 possible
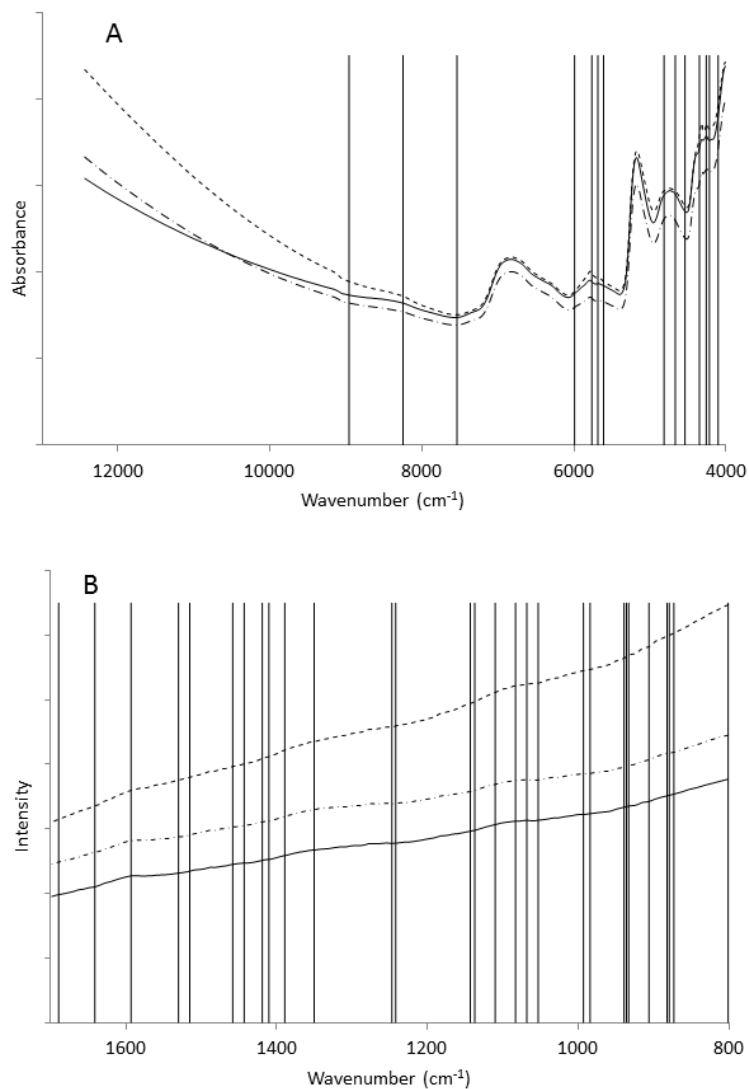
Figure 3.2: Average NIRS (A) and Raman (B) spectra from feces of animals fed BW $-\cdot$, Sudan $-$, and Timothy $--$ hays with no mesquite. Vertical lines show the location of wave numbers selected for canonical discriminant analysis.

wavenumbers for Raman spectra met the $P \leq 0.05$ entry and staying criteria for the stepwise discriminant procedure (Table 3.3).

Canonical discriminant analysis of the wavenumbers selected in the stepwise procedure showed that Raman and f.NIRS spectra could classify all observations with 100% accuracy and that separation of diets was greater for Raman spectra compared to f.NIRS spectra (Figure 3.3). All test data sets were also classified with 100% accuracy (data not shown). Coefficients of the canonical discriminant functions of Raman spectra showed that lignin and hemicellulose were the most important variables for both the first and second discriminant functions (Table 3.3). The first canonical discriminant function equally separated BW, Sudan and Timothy and the second discriminant function further separated Sudan from BW and Timothy (Figure 3.2B). Coefficients of the canonical discriminant function of f.NIRS spectra showed that starch, protein and oil were the most important variables for the first canonical discriminant function (75% of variation), which primarily separated BW and Sudan from Timothy. The most important canonical coefficients on the second function (25% of variation) for f.NIRS spectra were associated with lipid and cellulose and separated BW from Sudan on this axis. Linear discriminant functions for Raman spectra indicated that classification of BW and Sudan diets was based on lignin peaks but at different wavenumbers. Classification of Timothy was also based on lignin but hemicellulose and carotenoids were also important. Linear discriminant functions for f.NIF spectra showed that classification of BW and Sudan diets was based on protein and lipid peaks but at different wavenumbers. Classification of timothy was based on lignin, starch and water peaks.

Discussion

The improvement in validation statistics for the f.NIRS spectra obtained by adding two additional factors was presumably because the additional factors accounted for matrix effects caused by different base diets on the spectra. This sug-
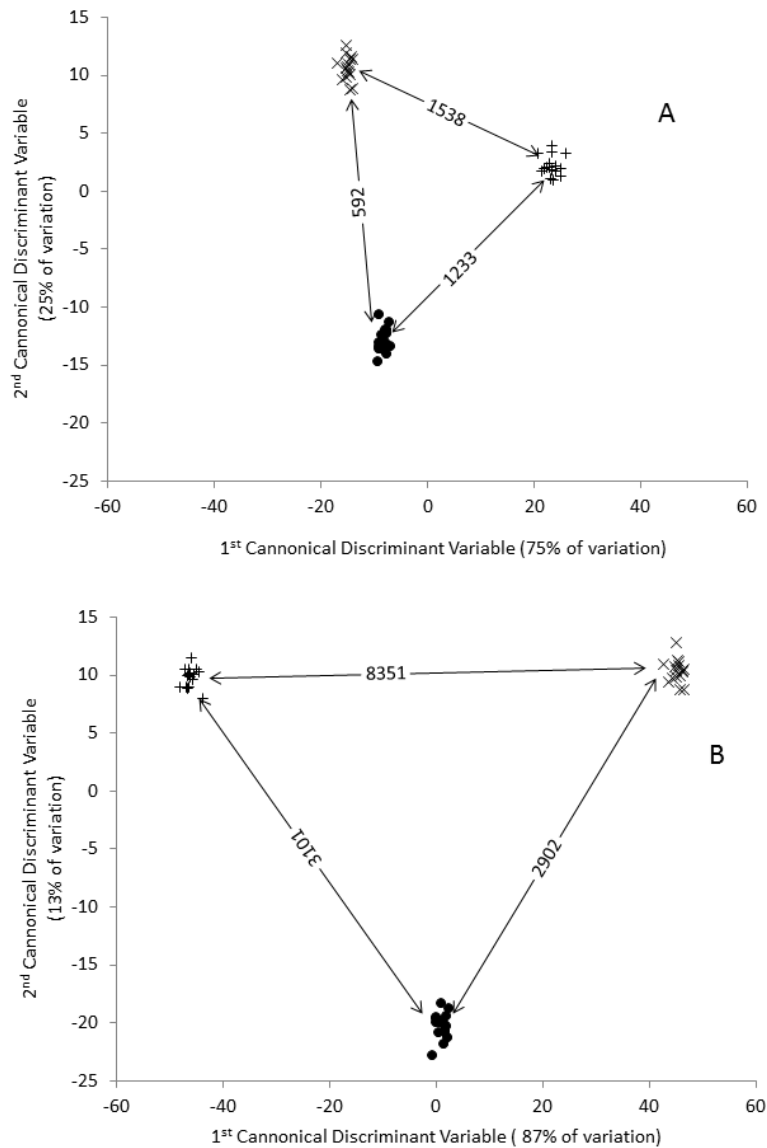
Figure 3.3: Plot of canonical discriminant scores from discriminant analysis of f.NIRS (A) and Raman (B) spectra to discriminate among hay diets: × BW; ● Sudan; + Timothy. Axes show percent of variation in spectra accounted for by each Eigenvector. Double headed lines show the squared Mahalanobis distance between the center of each group.

gests that when predicting independent samples whose base diets differ from the calibration diets, the usual case for fecal diet calibrations, increasing the number of factors above the optimal number indicated by cross validation may be useful. This may be particularly applicable when the number of factors in the calibration model is small as was the case in this study. The RPD values for cross validation (1.8) and validation (2.6) indicate that the former would be useful for distinguishing between high and low values, and the latter for approximate quantitative predictions [59]. These results indicate that f.NIRS is a viable method for estimating consumption of mesquite in the diets of cattle, and are considered quite good because previous studies [69] that used f.NIRS of diet fecal pairs had much wider ranges in the percentage of the plant species in the diet used for calibration. In that study, four different species were investigated and range of percentages of the species in the diets was a minimum of 24 percentage units and a maximum of 100 percentage units, compared to this study that had a range of only 5 percentage units for mesquite. Cross validation R^2 were all above 0.90 and RMSE ranged from 1.9-5.6 percentage units in the previous study [69] compared to $R^2 = 0.70$ and RMSE = 1.11 percentage units for this study. The cause of the poor performance of Raman spectra did not spectroscopy for predicting percentage mesquite in the diets because there was no pattern in intensity of spectra at different levels of mesquite either within a hay or between hays. The cause of this is not clear. In contrast to the poor performance of Raman relative to f.NIRS for predicting percentage mesquite in the diet, Raman spectra were better able to discriminate among the base hay diets, which was not expected. The better discrimination by Raman was because there was a large differences in intensity for feces from the three hays (Fig 1B), while f.NIRS spectra often overlapped and crossed. Feeding mesquite at the 5% level resulted in a reduction of intake and diarrhea for some animals after the second day at this level. Baptista and

33

Launchbaugh [49] and also reported decreased intakes in diets above 5% mesquite. This indicates that feeding low levels of mesquite could affect rumen function and animal physiology resulting in a reduction of even at subclinical levels of intake. The metabolic effects of consuming mesquite could cause matrix differences in feces that were detected by f.NIRS but not Raman. Near infrared spectroscopy is sensitive to physical differences in scanned materials [71] while Raman spectroscopy is not, which may explain why useful calibrations for percentage of mesquite in the diet could be developed for f.NIRS spectra but not Raman spectra. Differences in the canonical discriminant analysis of Raman and f.NIRS spectra provide insight into the differences between these two spectroscopic techniques. Discrimination using Raman spectra was primarily associated with wavenumbers associated with undigestible constituents of the diet (i.e., lignin). In contrast, discrimination using f.NIRS spectra was primarily associated with wavenumbers associated with digestible constituents in the diet (i.e., protein, starch and lipid). Raman spectroscopy is most commonly used to identify specific chemical compounds based on well-defined spectral bands; however, in this study, similar to f.NIR, the differentiation of different hay diets by Raman spectra was the result of differences of spectral intensity between feces from animals consuming different hays. This study was originally designed to produce fecal diet pairs for collecting f.NIRS spectra. The availability of a Raman spectrometer for comparison was discovered after the feces had been prepared for f.NIRS analyses.

Implications

This study showed that f.NIRS has the potential to, at a minimum, predict high and low consumers of chemically defended plants such as mesquite that are only consumed in small amounts. This information can be used to help select animals that have a higher intake of these plants and thus have a greater potential to more effec-

tively utilize the vegetation in areas where species such as mesquite are abundant. This is the first study to demonstrate that Raman spectroscopy has the potential for discriminating among animals that are consuming different diets. Because in contrast to NIR, water does not affect Raman and because field friendly, hand held Raman spectrometers, such as the one used in this study, are readily available, this technology has a great potential for ecological field studies. NIRS spectroscopy has shown great potential in ecological studies [53, 66]. We believe that Raman spectroscopy has a similar potential and deserves further investigation as a quantitative technique in ecological field studies.

Table 3.2: Calibration, cross validation and validation statistics for partial least squares regression of NIRS and Raman spectra to predict percentage mesquite in cattle diets.

	Method	Mean	Stdey	Factors	Slope	Intercept	R^2	RMSE	SEP	Bias	RPD
Calibration	NIRS	2.56	1.80	3.00	0.78	0.55	0.78	0.93	0.95	0.00	2.1
	Raman	2.56	1.23	3.00	0.37	1.61	0.37	1.59	1.61	0.00	1.3
Cross Validation	NIRS	2.57	1.77	3.00	0.73	0.71	0.70	1.11	1.12	0.01	1.8
	Raman	2.68	1.13	3.00	0.02	2.62	0.00	2.16	2.19	0.12	0.9
Validation	NIRS	2.06	2.26	5.00	1.03	1.88	0.88	2.09	0.78	1.95	2.6
	Raman	4.99	1.44	3.00	-0.32	5.80	0.21	3.80	3.00	2.43	0.7

Table 3.3: Standardized canonical coefficients of discriminant functions based on Raman and NIRS spectra of cattle feces for discriminating between base hay diets. Spectra are listed in order of importance of the coefficient (i.e., absolute value) to the discriminant function. Compounds are the compounds associated with the wavenumber (WN).

	Raman				NIRS		
WN(cm^{-1})	Coeff 1	Coeff 2	Compound	WN (cm^{-1})	Coeff 1	Coeff 2	Compound
936	9770	-17390	Lignin[48]	2370	404	137	Starch[71]
933	5265	8095	Lignin[48]	2346	-386	-173	Protein[73]
939	3350	8458	Lignin[48]	1212	-270	55	Lipid[71]
1242	1444	773	Hemicellulose[48]	2316	186	-146	Starch[71]
1257	1342	-627	Pectins[52]	1326	159	13	Lignin[64]
882	-996	-2115	Hemicellulose[62]	116	127	-58	Water[71]
906	996	151	Cellulose[70]	1668	-121	-23	Protein[62]
1443	970	392	Lipids/Fatty Acids [62]	1782	100	156	Cellulose [73]
1530	-931	-117	Carotenoids [62]	1734	-98	175	Hemicellulose[50]
993	891	2014	Cellulose[70]	1758	86	-388	Lipids[71]
1419	737	1244		2142	72	-246	Lipids[73]
984	-645	-489	Xylan[48]	2202	-63	123	Lignin[73]
801	604	393	Lignin[57]	2076	-19	174	Cellulose[63]
1458	543	-943	Cellulose[73]	2298	-18	268	Cellulose[73]
873	523	1094	Hemicellulose[55]				
1410	402	-314	Cellulose[70]				
1110	383	122	NCS polysaccharides[56]				
1137	-362	4	Lignin[48]				
1389	-280	-382	Lignin[48]				
1515	-241	300	Lignin[48]				
1053	228	591	Cellulose[70]				
1083	-227	623	Starch [55]				
1143	-165	-272	Cellulose [61]				
1641	40	474	$\alpha-pinene$ [62]				
1689	33	-152					

37

COHERENT ANTI-STOKES RAMAN SPECTROSCOPY: UNDERSTANDING THE ESSENTIALS *

This section is a brief overview to coherent anti-Stokes Raman spectroscopic technique and introduces the strengths and barriers to its use all based on the interpretation of simple theoretical formulae. The application of the Gaussian ultrashort pulses as a practical elucidatory reconstruction tool in the extraction of coherent Raman resonant spectra from the overall data contaminated with the non-resonant four wave mixing background is highlighted. The section presents the integral formulae for coherent anti-Stokes and Stokes Raman scattering, and discusses the closed-form solutions, its complex error function, and the formula for maximum enhancement of the inferred pure coherent Raman spectra. As an example, the time-resolved coherent Stokes Raman scattering experimental observations are quantitatively elucidated. Understanding the essentials of coherent Raman spectroscopy, therefore, promotes the importance of a number of experiments including the ones utilizing a broadband excitation with a narrowband delayed probing for successful background suppression.

Introduction

A spectroscopic technique based on coherent anti-Stokes Raman scattering (CARS) was first demonstrated by Maker and Terhune in [74]. CARS spectroscopy is a powerful technique which has been widely applied essentially in interdisciplinary research fields on the borders of biology, chemistry, physics, healthcare, defense, remote sensing, forensics, material science and so on. The recent breakthrough achievements

---

such as detection of bacterial spores [23, 24], implementation of coherent Raman microscopy [75, 76], gas-phase thermometry of reacting and non-reacting flows [77] and many others have been its state-of-art successes. There many reviews on CARS have been published [78, 79, 80, 81, 82, 83, 84, 85, 86, 87, 88, 89, 90, 91, 92, 93]. Particularly, a CARS bioimaging capability has been briefly reviewed most recently by Camp Jr and Cicerone in [88], and an extended overview of the the cutting-edge technologies of the practical CARS microscopy has been edited by Chen and Xie in [87]. Its chemical imaging applications in biology and medicine and specially for cancer, have been systematically evaluated in [81, 89, 90]. Moreover, Ellis and others have thoroughly discussed both the Raman and CARS spectroscopy as a diagnostic tool in biomedicine [85]. CARS applications in homeland security have been mentioned in the Raman spectroscopy review [84]. CARS spectroscopic diagnostics of nonequilibrium plasmas and flows have been given in a topical review [86], in addition to the review by Roy, Gord and Patnaik in [77]. Considering the amount of good reviews widely accessible it is not our intention to list all developments on CARS spectroscopy. Rather, this section focuses on the common CARS techniques which apparently bear many different names referred to as background-free CARS, FAST CARS, hybrid CARS, broadband CARS, multiplex and time-resolved CARS. In spite of the diversity in naming, all of these have one unique feature—they all use a broadband excitation together with a narrowband delayed probe pulse [23, 24, 94, 95, 96, 97, 98, 99, 100, 101, 102]. As mentioned by Scully and others in [103] implementation of ultrafast laser pulses is most crucial here. Generally two pulses (called as pump and Stokes) excite molecular Raman vibrations and a third pulse (called as probe) then scatters off from these coherently vibrating molecules. The scattered photon energy increased or decreased by an amount of Raman frequency. In coherent anti-Stokes Raman scattering, the scattered light wavelength is
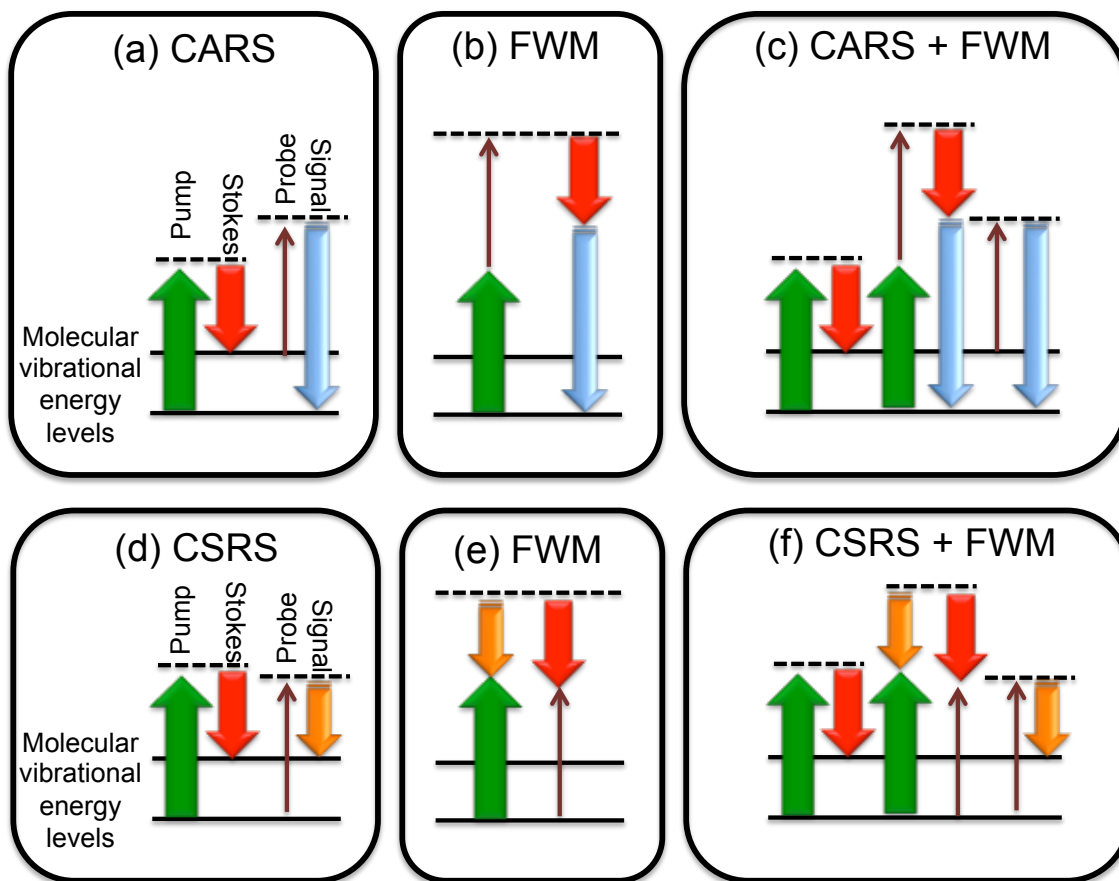
Figure 4.1: A schematic diagram of CARS and CSRS processes. (a) CARS. The scattered light in CARS is blue-shifted. (d) The scattered light in CSRS is red-shifted. (b,e) FWM. It is the third order nonlinear non-resonant process nothing to do with molecular Raman vibrations. (c,f) The overall measured data can not distinguish CARS/CSRS from FMW.

shifted into blue. A schematic diagram of CARS process is shown in Figure 4.1(a). The scattered light in coherent Stokes Raman scattering (CSRS) is red-shifted, see Figure 4.1(d). To distinguish the two processes, CARS and CSRS are referred explicitly, in the rest of the section. The pump and Stokes pulses simultaneously excite and prepare molecules in coherent state. With or without delay, the probe pulse comes in, and as a result anti-Stokes/Stokes signal is generated. Unfortunately, four wave mix-

ing (FWM) contamination is unavoidable. FWM is the third order nonlinear process that does not depend on molecular Raman vibrations, see Figure 4.1(b,e). FWM is added and mixed as a non-resonant background noise in the overall measured spectral data, see Figure 4.1(c,f). Therefore, it is extremely important to extract pure resonant (CARS/CSRS) information from the overall data contaminated with FWM. This issue will be studied in detail later. Even though there have been a number of methods suggested to suppress FWM non-resonant background, the aforementioned few specifically selected experiments with broadband (fs) pump and Stokes excitation pulses with a narrowband (ps) shaped and delayed probe pulse have been successfully demonstrated [23, 24, 94, 95, 96, 101, 102, 98, 99, 100, 97]. First of all, broadband pump and Stokes pulses excite multiple Raman vibrations at once, providing fingerprint signature recorded at a single laser shot level. A rapid bacterial spores detection, in this sense, is the key advantage as demonstrated in [24]. Second, narrowband probe utilization provides sufficient spectral resolution for Raman spectra of the target material. Most Raman linewidths are less than tens of wave numbers. Third, delayed probing with respect to the excitation ensures highly suppressed FWM. Last, but, perhaps, the most important (seemingly "hidden") advantage of enhancement will be discussed later. Specific probe shapes in time- and frequency-domain have been adapted including sinc-square [23, 94, 24, 96, 101, 102], square-sinc [98], exponential-Lorentzian [100, 101, 102, 99] and Gaussian-Gaussian [104, 97] forms. However, while all these experiments demonstrated adequate suppression of unwanted FWM to the extent of a certain degree (only at fixed time delay), an extraction of pure CARS/CSRS contribution in the entire spectrogram for arbitrary probe delay turns out to be quite cumbersome. This requires the "blind" numerical simulations usually with far less physical insight of actual ongoing processes. To overcome this challenge, the approximate closed-form solutions with all above-mentioned

pulse shapes have been obtained in [105, 106]. These approximate solutions are more appropriate for particularly impulsive CARS. The impulsive CARS experiments in which a common broadband excitation pulse (that contains both pump and Stokes portions with degenerate center frequencies) accompanied with a delayed narrowband probe pulse, have been reported in [98, 107, 97]. This demands a simple deductive extraction tool for the time-resolved CARS/CSRS. This challenge has been tackled (at least, in part) by the authors [104]. All Gaussian pulse shapes are the simplest, thus, the exact solutions both for CARS and CSRS have been easily obtained.

The Gaussian formalism is indeed the best tool for the present section's purpose as well. This section is an extension of our early work [104] and comprehensive illustrations towards the essential features of time-resolved coherent Raman spectroscopy are given here. The section consists of three more sections. First section is the main one where a simple theory for CARS and CSRS is introduced with elucidative approach. We hope that after getting well-armed with this theory, one can easily interpret typical experimental observations and understand their importance in Raman spectroscopy focused scientific community. Thus, several relevant experimental observations and realizations of long probe pulse will be discussed in the following section. Finally, we will summarize.

Theoretical Background

A simple comprehensive theory for CARS and CSRS is introduced in this section. It begins with CARS formulation and, based on obtained solutions, a newly recognized (somewhat neglected in the past) effect such as enhancement in coherent Raman spectroscopy at positive probe delay is introduced in detail. At the end of this section, the experimental observations are elucidated with the CSRS formulation.

Coherent Anti-Stokes Raman Scattering

Integral Formula

Let us start with a theoretical description of the third-order nonlinear process. The overall time-resolved signal amplitude – $P^{(3)}(\omega_{aS}, \tau)$ is expressed as a sum of the FWM – $P^{(3)}_{FWM}$ and CARS – $P^{(3)}_{CARS}(\omega_{aS}, \tau)$ amplitudes. The explicit integral forms are obtained in [104] expressed as

$$
\begin{aligned}
P^{(3)}_{CARS}(\omega_{aS}, \tau) &= \int_{-\infty}^{\infty} d\omega \left(\sum_{j}^{N} \frac{\alpha_j E_3(\delta_{aS} - \omega, \tau)}{\Delta_j - \omega - i\Gamma_j/2} \right) \int_{-\infty}^{\infty} d\omega' E_1(\omega') E_2^*(\omega' - \omega) \\
P^{(3)}_{FWM}(\omega_{aS}, \tau) &= \alpha_0 \int_{-\infty}^{\infty} d\omega E_3(\delta_{aS} - \omega, \tau) \int_{-\infty}^{\infty} d\omega' E_1(\omega') E_2^*(\omega' - \omega) \\
P^{(3)}(\omega_{aS}, \tau) &= P^{(3)}_{FWM}(\omega_{aS}, \tau) + P^{(3)}_{CARS}(\omega_{aS}, \tau)
\end{aligned} \tag{4.1}
$$

Here α_0 and α are constant complex coefficients. $E_{1,2,3}$ are electric fields for pump, Stokes and probe ultrashort pulses with the corresponding center frequencies $\omega^0_{1,2,3}$, whereas ω_{aS} and τ are the frequencies of the anti-Stokes signal and probe delay, respectively. The other parameters are Raman vibrational frequency – Ω_R, Raman detuning – $\Delta = \Omega_R - (\omega_1^0 - \omega_2^0)$, center frequency of anti-Stokes signal – $\omega_{aS}^0 = \omega_3^0 - \Delta\omega^0$ and CARS detuning – $\delta_{aS} = \omega_{aS} - \omega_{aS}^0$. Although, a rigorous CARS theory has been developed in many textbooks, reviews and research papers (for some, see [108, 110, 87, 111, 79, 112, 113]), the simplest possible CARS formulation is currently our intention. For the sake of simplicity, it is assumed that the phase matching condition is satisfied and any other explicit propagation contributions are discarded in derivation of Eq.(4.1). Later, by comparing the theoretical and experimental results it is shown that this simplification is accurate to elucidate the essential ingredients of coherent Raman spectroscopy. The complete version of the CARS integral formula was first derived in [104], which is a generalization of the ones given for impulsive

CARS in [105, 106].

As stated in [104], Eq.(4.1) is in its best form due to appropriate choice of integration variables. For instance, the variables weighing around zero and varying from negative to positive infinities do help in obtaining the closed-form solutions that include Gaussian integrals. That is convenient, especially if all input pulses are Gaussian. For all Gaussian pump, Stokes, and probe pulses, the exact closed-form solutions of Eq.(4.1) are found in [104] as to be

$$P_{CARS}^{(3)}(\omega_{aS}, \tau) = -iW_{12}e^{-\frac{\tau^2}{2t_{FWM}^2}}e^{-2ln2\frac{\delta_{aS}^2}{\Delta\omega_{FWM}^2}}e^{i\delta_{aS}\frac{\Delta\omega_3^2}{\Delta\omega_{FWM}^2}\tau}\sum_{j=1}^{N}\alpha_j'w(\zeta_j)$$

$$P_{FWM}^{(3)}(\omega_{aS}, \tau) = \alpha_0'W_{12}W_{123}e^{-\frac{\tau^2}{2t_{FWM}^2}}e^{-2ln2\frac{\delta_{aS}^2}{\Delta\omega_{FWM}^2}}e^{i\delta_{aS}\frac{\Delta\omega_3^2}{\Delta\omega_{FWM}^2}\tau}$$

$$P^{(3)}(\omega_{aS}, \tau) = P_{FWM}^{(3)}(\omega_{aS}, \tau)\left(1 - \frac{i}{\alpha_0'W_{123}}\sum_{j=1}^{N}\alpha_j'w(\zeta_j)\right) \tag{4.2}$$

$A_{1,2,3}$ are the amplitudes of the input Gaussian pulses. The other parameters here include slightly modified coefficients – $\alpha_0' = \pi\alpha_0 A_1 A_2^* A_3/4ln2$ and $\alpha_j' = \pi^{3/2}\alpha_j$ $A_1 A_2^* A_3/\sqrt{8ln2}$, spectral full widths at half maxima (FWHMs) – $\Delta\omega_{1,2,3}$ and the others – $W_{12}^2 = \Delta\omega_1^2\Delta\omega_2^2/(\Delta\omega_1^2 + \Delta\omega_2^2)$, $W_{123}^2 = (\Delta\omega_1^2 + \Delta\omega_2^2)\Delta\omega_3^2/\Delta\omega_{FWM}^2$, $\Delta\omega_{FWM}^2 = \Delta\omega_1^2 + \Delta\omega_2^2 + \Delta\omega_3^2$, and $t_{FWM} = \sqrt{4ln2}/W_{123}$.

The solution for the transient FWM $P_{FWM}^{(3)}$ is understood as follows. As seen from Eq.(4.1), it is a product of two Gaussian functions: one with a temporal width t_{FWM} and depends on probe delay τ, centered at zero delay; the other one with a spectral width $\Delta\omega_{FWM}$ and that depends on the CARS detuning δ_{aS}. In the case of broadband pump or Stokes and narrowband probe pulses the width of the

44
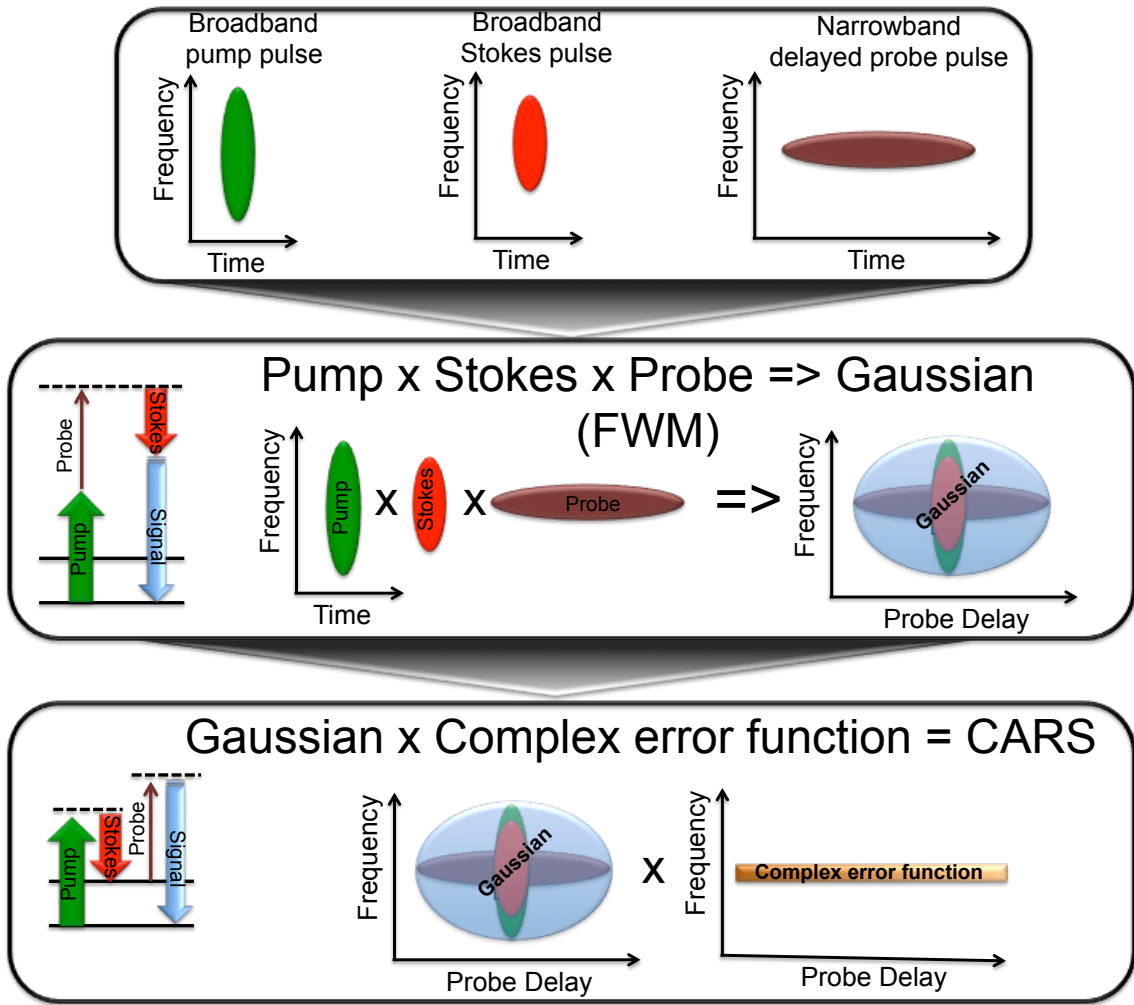
Figure 4.2: Interpretation of the solutions. The broadband pump or Stokes pulse defines the spectral width of Gaussian solution for FWM. A narrowband probe pulse time duration defines temporal width of Gaussian solution for FWM (top and middle). FWM solution is a product of two Gaussian functions (middle). CARS solution is a product of FWM and the Faddeeva function depending on Raman line width. This suggests an efficient FWM suppression at probe delay comparable to its time duration.

pump/Stokes pulse mainly determines $\Delta\omega_{FWM}$ and probe pulse duration determines t_{FWM}, see Figure 4.2. Assuming $\Delta\omega_1 \approx \Delta\omega_2 \gg \Delta\omega_3$ we obtain $\Delta\omega_{FWM} \sim \Delta\omega_1$ (i.e., pump/Stokes spectral width). Thus $W_{123} \sim \Delta\omega_3$ we also obtain $t_{FWM} \sim 1/\Delta\omega_3$ (i.e.,

probe temporal width). This means that if probe pulse is delayed for a period of time at least comparable to its temporal width, then FWM is efficiently suppressed in a simple way as for Gaussian function. However a question arises if CARS signal would still be present at this delay. This will be explained later. The solution for CARS is a product of the same Gaussian functions in the FWM solutions and the Faddeeva function [114, 115, 116] $w(\zeta)$ with complex argument ζ. The Faddeeva function is an error function with a complex argument. In our case, the argument of the Faddeeva function is given by $\zeta_j = [(\delta_{aS} W_{123}^2/\Delta\omega_3^2 - \Delta_j + i\Gamma_j/2)t_{FWM} - i\tau/t_{FWM}]/\sqrt{2}$ where Γ_j are FWHM of the jth Raman line. For the impulsively excited CARS, in the limit $W_{123} \to \Delta\omega_3$, this expression reduces to the one found earlier in [105, 106]. Depending on material, Raman line widths Γ_j are different. Those Raman lines, narrower than the probe width, dephase much slower and still survive at much long delay (e.g., for molecules in gas-phase). The Faddeeva function for a chosen narrow Raman line is sketched in Figure 4.2, in the bottom. Once again, the CARS signal can be interpreted as a product of FWM and the Faddeeva function. There is a common delay dependent phase $\delta_{aS}\tau\Delta\omega_3^2/\Delta\omega_{FWM}^2$ in both the FMW and CARS solutions. This will not affect the measured sum spectra which is expressed with the modulus square of amplitudes as $|P^{(3)}(\omega_{aS}, \tau)|^2 = |P_{FWM}^{(3)}(\omega_{aS}, \tau) + P_{CARS}^{(3)}(\omega_{aS}, \tau)|^2$. The spectrogram data is a collection of spectra at each probe delay. As for example, the normalized spectrogram for FWM, CARS and their sum with a single Raman line are shown in Figure 4.3 for three different probe pulse widths: the two are 4 and 20 times broader than the remaining one. As mentioned previously, the FWM temporal width increases as probe pulse gets longer. On one hand, the FWM spectrograms are in the form of Gaussian functions. On the other hand, pure CARS spectrograms are governed mainly by the Faddeeva function defined by a Raman line width and becomes narrower as probe width further decreases. The spectrograms for sum of
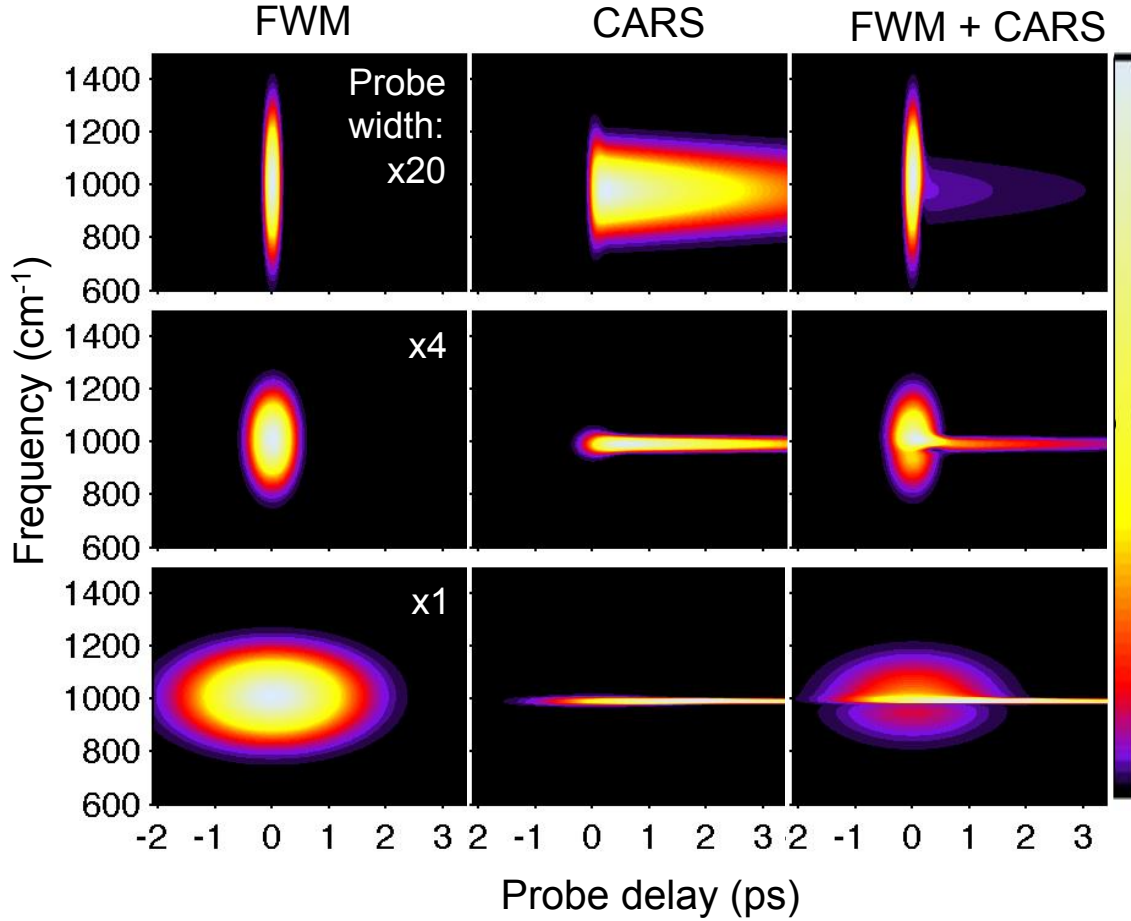
Figure 4.3: Normalized spectrograms for FWM, CARS and their sum. The narrow-band probe is increased 4 and 20 times. The results are obtained from Eq.(4.2) for a single Raman line.

FWM and CARS are shown on the right side of Figure 4.3. Around zero delay relative phase between FWM and CARS signal amplitudes comes into play. The extraction method of Raman spectrum from the sum spectrum at zero delay is possible. The method based on Kramers-Kronig relation has been developed and implemented, for instance, in [117, 118]. At this point, the present theory can also be understood as a CARS "extraction" tool in the entire positive delay region. The procedure can be listed as follows: (i) compare the normalized theoretical sum spectrogram

to the normalized experimental data (ii) obtain all physical parameters including the ones for input pulses and material; and lastly (iii) deduce CARS signal alone with these parameters. This will be shown later for pyridine data. Because the normalized data are considered, the input pulse energies are less important than the pulse widths, time durations, and center frequencies. The molecular parameters include the Raman line width, polarizability, third order nonlinear susceptibility, and Raman cross section. Therefore, we have no doubt that this tool will be considerably used in future, because of its simple yet informative nature. Moreover, it is important to note that one still cannot get rid of FWM if the probe width is too narrow, even narrower than Raman line. For example, in some material, Raman line is a sum of many lines and it can be quite broad. At the same time, too broad probe pulse is also a problem for discrimination a Raman peak against FWM background. An optimization of probe pulse for the best background-suppressed signal is discussed next.

Enhancement

It was mentioned in our earlier works [104, 24] that CARS signal is maximized at some positive delay, but not at zero delay. This effect is more pronounced for relatively long probe pulse. From physical point of view, this can be understood as follows. The pump and Stokes pulses prepare molecules in the coherent state. After excitation this molecular coherence eventually fades away within decoherence time. At zero delay, only fraction of photons (in the probe tale part) are scattered off the induced refractive index grating. The number of scattered probe photons, however, increases as the probe is delayed. As a result even more probe photons are overlapped and able to be scattered off. The threshold delay at which CARS signal maximized, thus, depends on the probe pulse duration and molecular decoherence

time. From mathematical point of view, the threshold delay time is determined as stationary point of the Faddeeva function. This effect is shown in Figure 4.4.
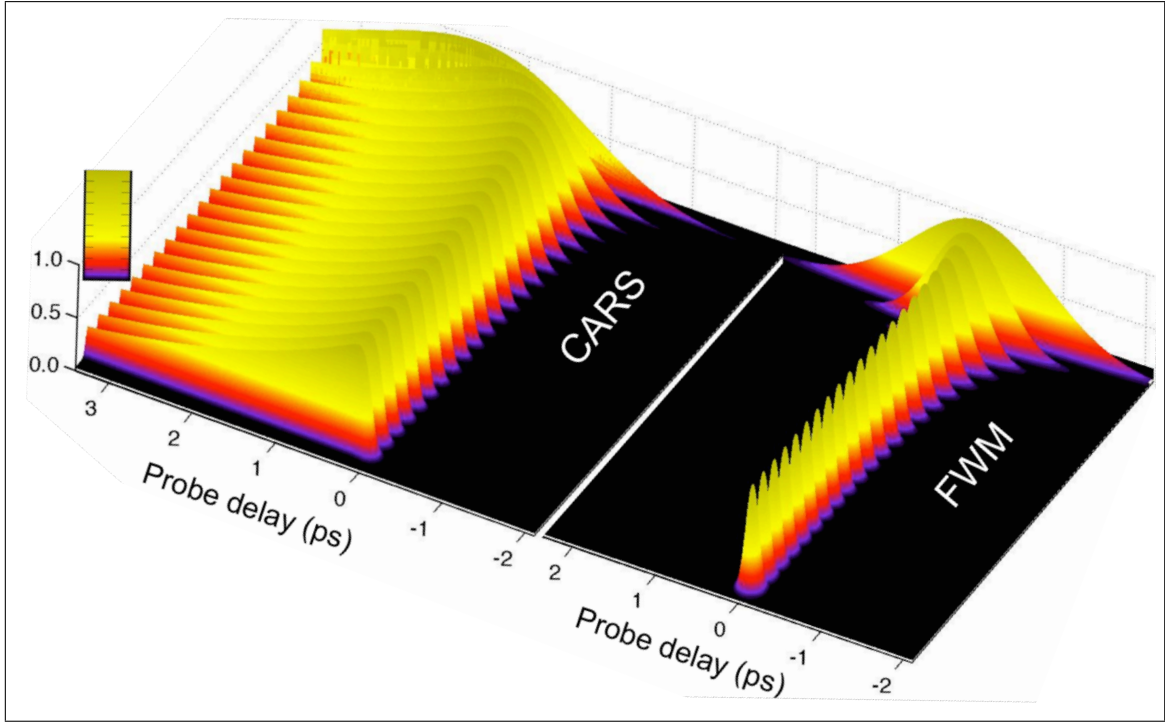
Figure 4.4: CARS enhancement at non-zero probe delay. Series of the normalized CARS and FWM signals using Eq.(4.1) depending on probe width and delay. This phenomenon is more obvious for narrower probe.

By varying probe pulse width, both CARS and FWM signals using Eq.(4.1) are plotted in series. Positions of FWM maxima do not alter, and remain at zero delay. However, as we expected, CARS maxima are shifted away from zero delay as probe width decreases. In principle, the threshold could be analytically determined from the stationary condition for the Faddeeva function. An accurate simple formula for the threshold time delay as a function of probe width and Raman line width is
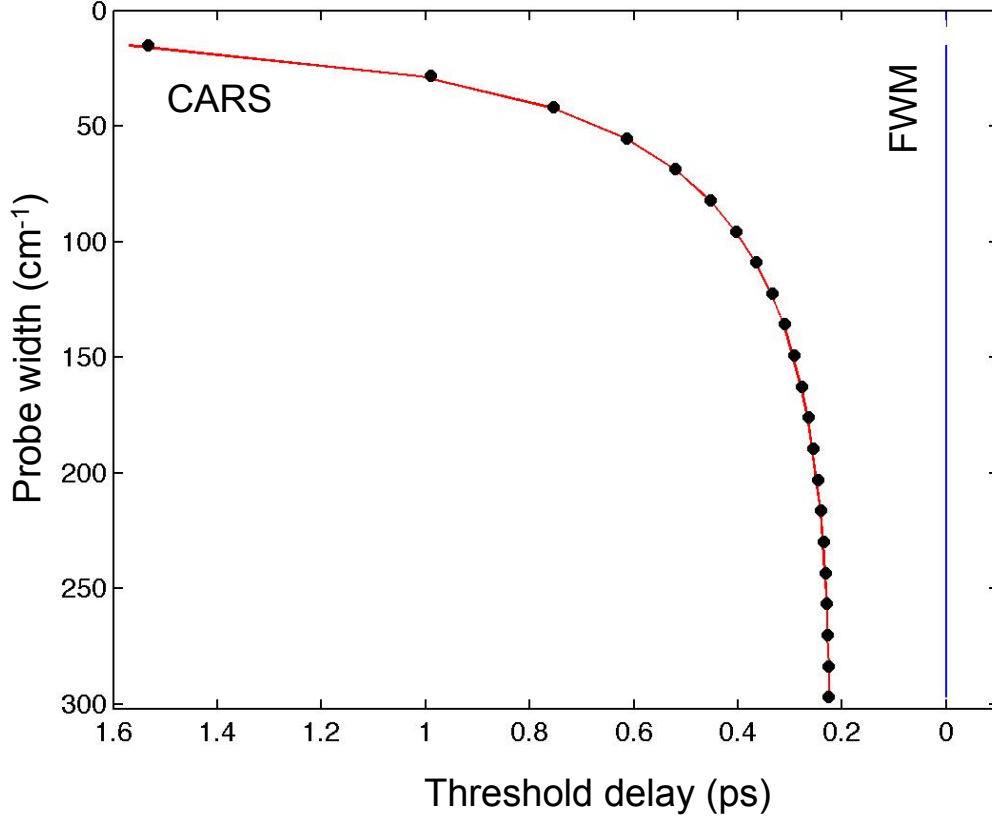
Figure 4.5: The threshold delay times are obtained from Eq.(4.3) as a function of probe widths. The analytic result (black dots) is compared to delays for maximum CARS (red solid curve) and FWM (blue straight line) signals.

obtained in [104] as

$$T_j^{threshold}(\Delta\omega_3, \Gamma_j) = t_{FWM} \left[\frac{1}{\varepsilon(\Delta\omega_3, \Gamma_j)} + \frac{\Gamma_j t_{FWM}}{2} \right] \qquad (4.3)$$

where ε is a linear function of inverse of the probe pulse width in the form of $\varepsilon = a\Gamma_j/\Delta\omega_3 + b$ with constant coefficients $a = 1.8$ and $b = 0.38$. The threshold time formula Eq.(4.3) is plotted (dots) as a function of probe pulse width in Figure 4.5. Solid curve is constructed from positions of CARS maxima from Figure

4.4. It is worth noting that although CARS enhancement at positive probe delay was previously mentioned briefly in [24, 105, 119, 120], an explicit formula Eq.(4.3) was obtained for the first time in [104].

Coherent Stokes Raman Scattering

The previous subsection is devoted to all about CARS where CARS process is formulated and its solution is obtained. The solution is explained in great detail with different aspects. For instance, a "legitimate" recognition of important CARS enhancement must be added to the current understanding of the successful demonstrations of those selected experiments [23, 24, 94, 95, 96, 101, 102, 98, 99, 100, 97]. The advantages of utilizing the broadband pump and Stokes excitation pulses with a narrowband shaped and delayed probe pulse must be updated as follows: (i) broadband pump and Stokes pulses excite multiple Raman vibrations simultaneously providing fingerprint signature achievable at single laser shot level; (ii) narrowband probe provides spectral discrimination of Raman spectra of the target material against FWM broadband background; (iii) delayed probing with respect to the excitation ensures highly suppressed FWM; and (iv) maximum CARS enhancement occurs at threshold probe delay, in most cases at a delay where FWM is highly suppressed. All above statements are also valid for CSRS, even though it is slightly different process that will be discussed here. In CSRS, the scattered light is red-shifted, see Figure 4.1(d). FWM contamination is again unavoidable in the overall measured data, see Figure 4.1(f).

Integral Formula and Its Solution

A convenient integral formula for CSRS has been derived (for the first time) by the authors. Following [104], the time-resolved total signal – $P^{(3)}(\omega_S, \tau)$ is a sum of

FWM – $P^{(3)}_{FWM}$ and CSRS – $P^{(3)}_{CSRS}(\omega_{aS}, \tau)$ contributions which are written as

$$P^{(3)}_{CSRS}(\omega_S, \tau) = \int_{-\infty}^{\infty} d\omega \left(\sum_j^N \frac{\beta_j E_3(\delta_S + \omega, \tau)}{\Delta_j - \omega + i\Gamma_j/2} \right) \int_{-\infty}^{\infty} d\omega' E_1(\omega' + \omega) E_2^*(\omega')$$

$$P^{(3)}_{FWM}(\omega_S, \tau) = \beta_0 \int_{-\infty}^{\infty} d\omega E_3(\delta_S + \omega, \tau) \int_{-\infty}^{\infty} d\omega' E_1(\omega' + \omega) E_2^*(\omega')$$

$$P^{(3)}(\omega_S, \tau) = P^{(3)}_{FWM}(\omega_S, \tau) + P^{(3)}_{CSRS}(\omega_S, \tau) \tag{4.4}$$

Here the frequency of the Stokes signal – ω_S, complex constant coefficients – β_0 and β_j, center frequencies of Stokes signal – $\omega_S^0 = \omega_3^0 + \Delta\omega^0$ and detunings for CSRS process – $\delta_S = \omega_S - \omega_S^0$ are used. A rigorous CSRS theory can be found, for instance, in [109, 121, 122], although, our approach (Eq.(4.4) and Eq.(4.1)) is simple, at the same time, the solutions are rich and informative. Once again, in derivation of Eq.(4.4), the phase matching condition is satisfied and any other explicit propagation contributions are discarded. In doing so, the solutions for Gaussian pulses are also found in [104] as

$$P^{(3)}_{CSRS}(\omega_S, \tau) = iW_{12} e^{-\frac{\tau^2}{2t^2_{FWM}}} e^{-2ln2\frac{\delta_S^2}{\Delta\omega^2_{FWM}}} e^{i\delta_S \frac{\Delta\omega_3^2}{\Delta\omega^2_{FWM}}\tau} \sum_{j=1}^N \beta_j' w(\zeta_j')$$

$$P^{(3)}_{FWM}(\omega_S, \tau) = \beta_0' W_{12} W_{123} e^{-\frac{\tau^2}{2t^2_{FWM}}} e^{-2ln2\frac{\delta_S^2}{\Delta\omega^2_{FWM}}} e^{i\delta_S \frac{\Delta\omega_3^2}{\Delta\omega^2_{FWM}}\tau}$$

$$P^{(3)}(\omega_S, \tau) = P^{(3)}_{FWM}(\omega_S, \tau) \left(1 + \frac{i}{\beta_0' W_{123}} \sum_{j=1}^N \beta_j' w(\zeta_j') \right) \tag{4.5}$$

The parameters are $\beta_0' = \pi\beta_0 A_1 A_2^* A_3/4ln2$ and $\beta_j' = \pi^{3/2}\beta_j A_1 A_2^* A_3/\sqrt{8ln2}$ and the Faddeeva function's argument is given by $\zeta_j' = [(\delta_S W_{123}^2/\Delta\omega_3^2 + \Delta_j + i\Gamma_j/2)t_{FWM} - i\tau/t_{FWM}]/\sqrt{2}$. One important difference between CARS and CSRS is that the Raman detuning comes with different signs inside the Faddeeva function's argument as $\zeta_j, \zeta_j' = [(\delta_{aS,S} W_{123}^2/\Delta\omega_3^2 \mp \Delta_j + i\Gamma_j/2)t_{FWM} - i\tau/t_{FWM}]/\sqrt{2}$. Moreover, an opposite sign in Eq.(4.5) and Eq.(4.2) suggests that the CSRS and CARS signal amplitudes

are out of phase. The CARS and CSRS comparative theory has been developed, for instance, in [122, 121] and the experimental observations of deviation between the two have been reported in [97]. Nevertheless these differences are not crucial for small Raman detuning, particularly if one investigates the two processes one at a time. In the experiment performed by Peng et al., in [97], the spectrograms for both CARS and CSRS signals are shown, see their reproduced results in Figure 4.6. In this experiment, a KML (85MHz rep. rate) mode-locked Ti:sapphire laser oscillator with the spectral FWHM $>$ 100 nm and the center wavelength of 810 nm was used for impulsive excitation of molecular vibrational modes. The oscillator output was focused onto a 5-mm-thick LBO crystal to produce the narrowband second harmonic generated light at a center wavelength of 405nm with $<$ 1 nm due to the phase-matching constraint. Note that the pulse shapes are considered to be Gaussian. This probes the induced coherent oscillations of the molecular ensemble. In Figure 4.6, the data correspond to neat solutions of benzene in (a,b) and pyridine in (c,d) and the CARS-CSRS spectrograms are shown in (a,c). For benzene CARS and CSRS are slightly different. The difference is clearly seen in the cross-sections of the spectrogram along the probe pulse delay at the peaks of CARS (blue solid curves) and CSRS (green dotted curves) in Figure 4.6 (b) and (c). For the excited benzene Raman mode 991 cm^{-1}, the CSRS data is suppressed compared to the CARS one whereas for pyridine, a mirror reflection symmetry is visible as expected previously in the theory. The beating pattern for pyridine data is a result of interference between two excited Raman modes, 991 and 1030 cm^{-1}, which will be discussed in the next subsection again.
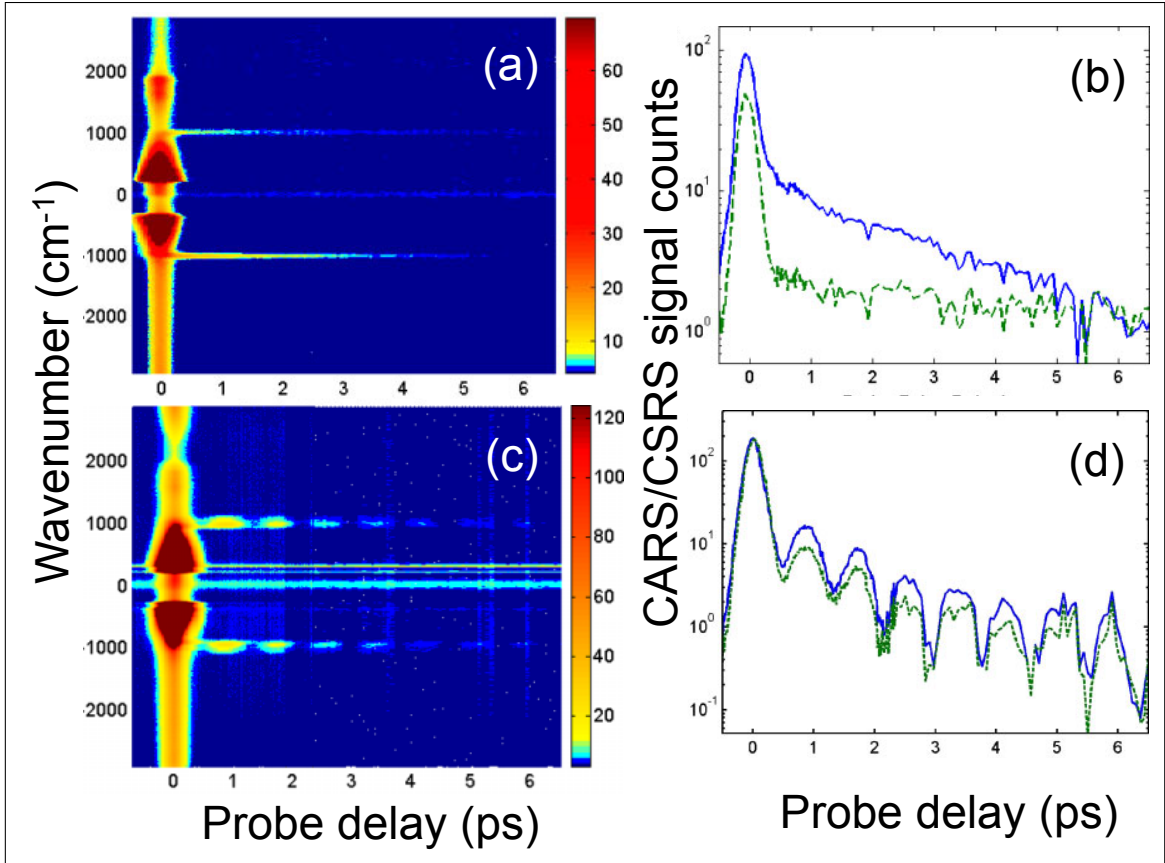
Figure 4.6: The data are reproduced from [97]. The CARS-CSRS spectrograms obtained on benzene and pyridine: (a,c) Spectra of the anti-Stokes and Stokes scattered light as functions of the probe pulse delay. The main part of the probe spectra were filtered by the notch filter; (b,d) Cross-sections of the spectrograms along the probe pulse delay at the peaks of CARS (blue solid curves) and CSRS (green dotted curves).

Reconstructing CSRS from the Observed Experimental Data

The theoretical results are presented here to compare to the experimental data. A one-to-one correspondence between them evidently supports our idea of inferring pure CSRS from real measured spectrogram data. However, we note that this approach is semi-empirical one. A true extraction based on only experimental observations is, however, even more demanding and far more important as it will be the

next step in the future. At the moment, by CARS/CSRS reconstruction, we mean the procedure that includes: (i) comparing theoretical results to the experimental data (ii) obtaining all physical parameters used in the theory; (iii) reconstructing pure CARS/CSRS signal alone with these parameters. For that matter, the one-to-one comparison between the normalized experimental and theoretical data are illustrated in Figure 4.7. The experiment performed for pyridine in liquid-phase. The Coherent Inc., Ti-sapphire amplified kilohertz laser system including the optical parametric amplifiers were used to generate broadband pump and Stokes pulses at designed wavelengths. The excitation was centered in the middle of molecular vibrational modes of pyridine. These Raman lines correspond to in-plane ring-bend 1030 cm^{-1} and ring-breathing 991 cm^{-1}. A separation of 39 cm^{-1} leads to a beating with a period of 0.855 ps if the probe pulse is broader compared to this separation. The widths of these lines are ~ 2.2 cm^{-1}. The dephasing lifetimes are about 2.55 ps for the one and slightly different ($\sim 20\%$) for the other, and Raman cross-sections are close [123, 124]. Width of the probe pulse was altered by a home-made 4f - pulse shaper with a closing slit placed on its Fourier plane. The data shown in Figure 4.7, were taken for three probe pulse widths: 300 cm^{-1}, 60 cm^{-1} and 15 cm^{-1}. For the 300 cm^{-1} broad probe, the Raman lines were not resolved which leads to a beating signal seen in the spectrogram (top left) as opposite to the narrowband 15 cm^{-1} probe that these lines are well resolved (bottom left). However, the probe width in between makes it difficult to access quantified information about period or separation (middle left). A theoretical comparison is depicted in the middle column of Figure 4.7. In the next column, the reconstructed CSRS is shown. Theoretical results are obtained from Eq.(4.4). The ratio of probe widths is consistent with the experimental choices. The other physical parameters including Raman line widths and their separation are chosen in the same way as for pyridine's real parameters. Particularly,
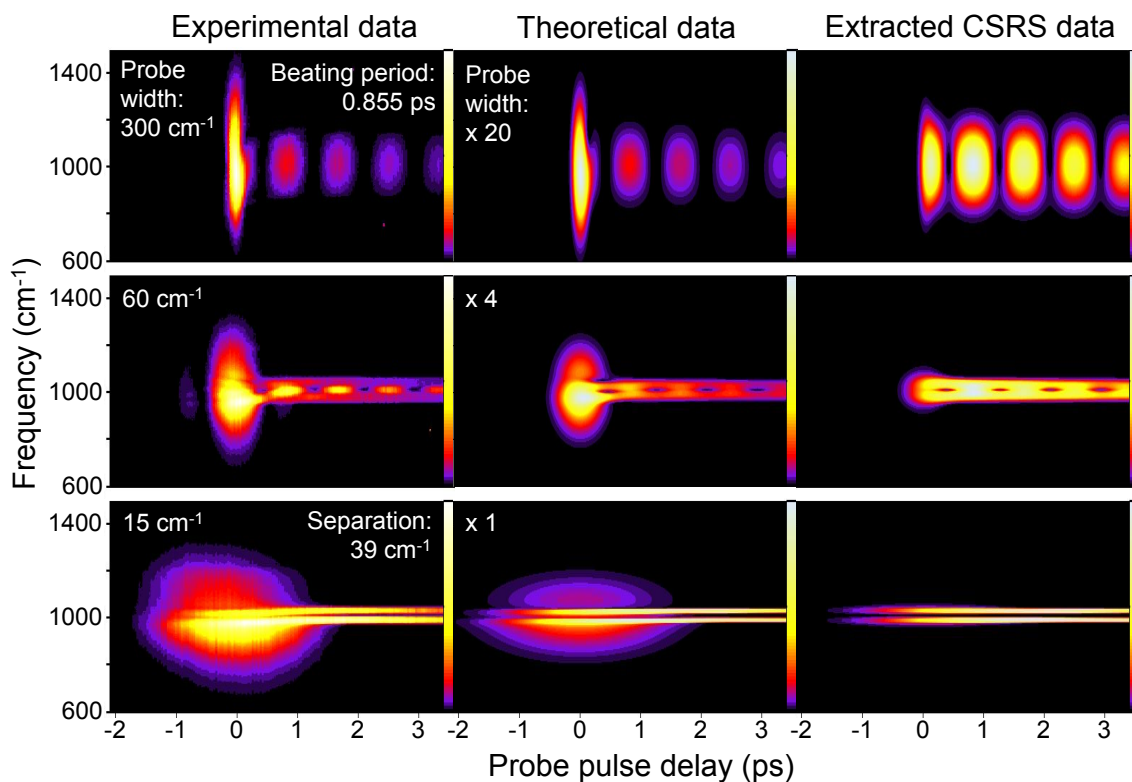
Figure 4.7: Reproduced from [104] with permission. Reconstruction of CSRS from experimental data. The experimental data (left column), theoretical results (center column), and reconstructed CSRS (right column). The experimental data were taken with probe pulse widths 300 cm^{-1}, 60 cm^{-1} and 15 cm^{-1}. A separation of Raman lines of pyridine molecules is 39 cm^{-1} with a beating period of 0.855 ps. Theoretical results for probe widths with ratio of 1, 4 and 20 obtained from Eq.(4.4). All physical parameters are equivalent to those for pyridine. Both theoretical and experimental data are normalized.

the two Raman line-widths differ by 20 % and a ratio between the Raman line-width and separation is equal to the ratio of 2.2 and 39 cm^{-1}. From the reconstructed CSRS with the narrowband probe (bottom right), two maximal enhancements at two slightly different threshold delays are found (around 1.5 ps). This is actually an important piece of information. For instance, position of the threshold delay alters depending on Raman line width for a given probe width according to formula

Eq.(4.3). In this sense, one can estimate Raman line-width more accurately: finding maximum position is much easier than fitting data with exponential decay and then deducing the line width. It is worth to bear in mind that for ps probe and molecules in gas-phase (for the isolated Raman lines), threshold delay is nevertheless far away from FWM; thus, formula Eq.(4.3) is still valid and accurate for the experimental data without even bothering to reconstruct CARS/CSRS. The situation becomes immediately complicated, if the Raman lines are not resolved. By the way, the more likely sinc-square (not exactly Gaussian) probe pulse shape was used in the actual experiment due to the home-made 4f-pulse shaper's nature. The normalized data analysis here ensures only main feature to be seen in coded colors. The normalized theoretical results with the Gaussian probe pulse, indeed, nicely fit the normalized experimental data, justifying that the dominant central lobe of the sinc-function (in time domain) is sufficiently approximated by a Gaussian function.

Experimental Realizations of Narrowband Probe Pulse in Background-Suppressed Coherent Raman Spectroscopy

In this section we discuss the experiments that utilize broadband excitations and narrowband delayed probe. This specific choice has the following advantages: (i) simultaneous excitation of multiple Raman modes; (ii) discrimination the Raman resonant CARS signals from non-resonant background FWM; (iii) suppression of FWM via probe timing; and (iv) enhancement of CARS signal via probe timing (from now on, by CARS we refer to both CARS and CSRS). Let us explain all these points separately in more detail. First, the pump and Stokes need to be broadband and thus, ultrashort in time domain (see, Figure 4.8). The broadband pump and Stokes allow access to excite multiple Raman modes at once, without a need of laser frequency tuning. A multichannel acquisition for multiplex CARS is

schematically shown in Figure 4.8, on the right column. The collimated scattered
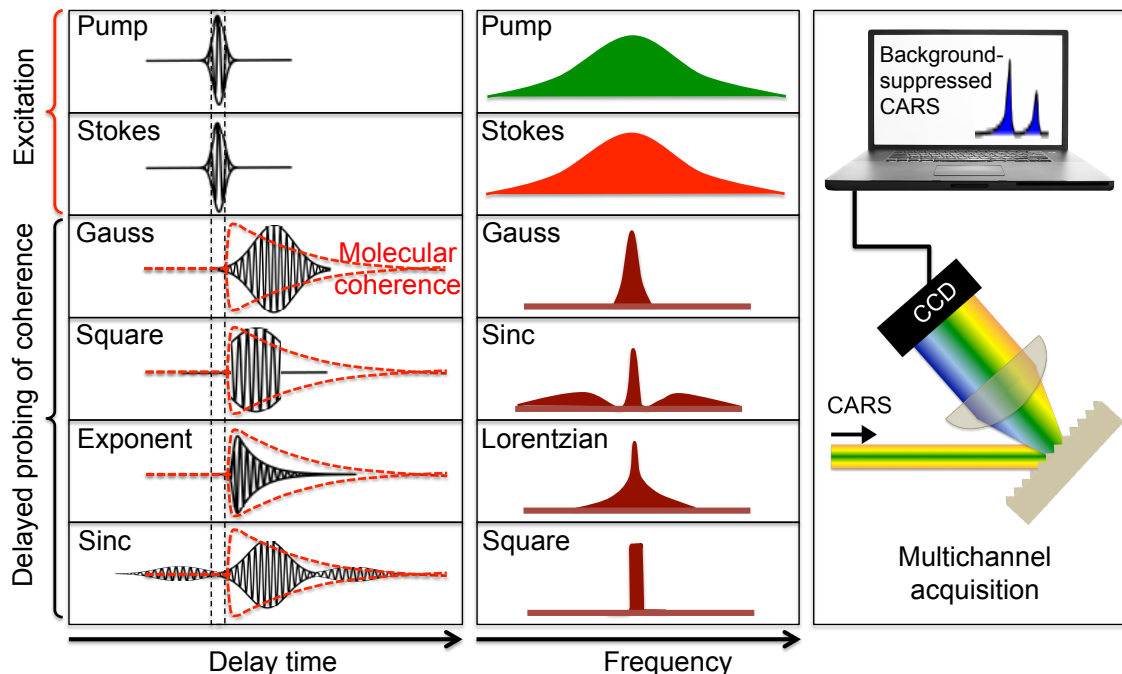
Figure 4.8: Input laser pulse shapes in time- and frequency domain. The excitation broadband pulses are Gaussian-Gaussian. Narrowband probe pulses including Gaussian-Gaussian, square-sinc, exponential-Lorentzian, and sinc-square and their delayed overlapping with an excited molecular coherence. Multiplex CARS spectra recording via multichannel acquisition with a grating and CCD camera.

CARS signal is dispersed by the grating. A lens images into CCD camera at the Fourier plane. The CCD image is further processed (recorded image is summed up vertically), calibrated with Raman shift in a unit of wavenumber, and displayed on the computer screen as Raman spectral data with several modes. The broader the excitation, the more Raman modes are covered, and the more information is gained for molecular analysis. This is essential for the specificity of the technique at single laser shot measurement [24]. Matter of fact, the excitation can be a single very broad

pulse span over pump and Stokes frequencies in the impulsive CARS.

Second, a narrowband probe resolves Raman peaks on the top of featureless FWM broadband background. In time-domain, probe must be long pulse. There are several realizations of narrowband probe starting with broadband pulse, see Figure 4.9. These include the following filters: (a) second harmonic generation (SHG) crys-
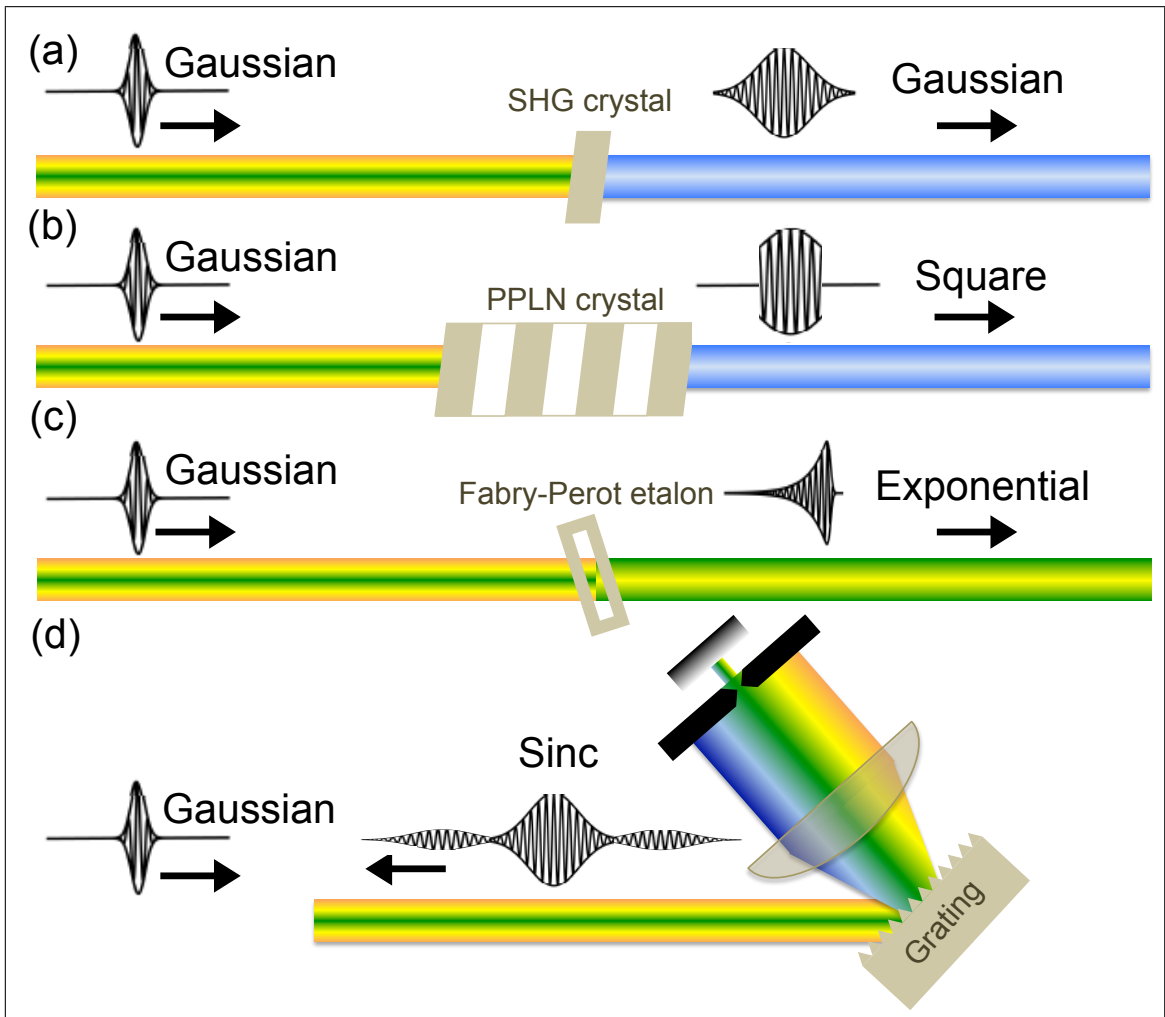
Figure 4.9: Realizations of narrowband probe pulses. The filters include (a) SHG crystal; (b) PPLN crystal; (c) etalon; and (d) grating for Gaussian-Gaussian, square-sinc, exponential-Lorentzian, and sinc-square shapes, respectively.

tal; (b) periodically poled lithium niobate (PPLN) crystal; (c) Fabry-Perot etalon; and (d) 4-f pulse shaper with a grating. All these methods convert fs broadband input pulses into ps – scale narrowband pulses. The generated pulse shapes typically have minor distortions except for the SHG crystal filter, which only narrows the input pulse width and, thus, prolongates its duration, see Figure 4.9(a). However, this prolongation is generally not sufficient for resolving Raman lines. The PPLN crystal is, in contrary, an efficient generator compared to the SHG all alone because phase matching condition is satisfied constructively. The output pulse shape in time-domain becomes square (or, top-hat), and in spectral domain, it is in the sinc function form. The central lobe of the sinc function spectrum is narrow and dominant, see Figure 4.8. A simple and straightforward method is to use a Lorentzian filter. That is essentially a Fabry-Perot etalon, i.e., just two parallel closely spaced partially transmitting (reflecting) mirrors. After multiple reflections, the output pulse is distorted in the exponential form. In frequency domain, the output pulse is, according to the fast Fourier transform (FFT), a Lorentzian which has a narrow central peak with long "mountain bottom", see Figure 4.8. The last filter involves a grating, Figure 4.9(d). In this case, input beam is initially dispersed in its color by the grating, then focused by a collimating lens. At the Fourier plane (at the focal plane) adjustable slit allows only portion of rainbow which is back reflected from the end mirror back to the grating. The portion determines a narrow (less than 1 nm) spectral characteristics of the output pulse. This is called a folded 4-f pulse shaper. The output pulse is in sinc function form in time domain and narrowband square in frequency domain, see Figure 4.8. The realizations and utilizations of the probe pulses in sinc (in time domain) and square (in frequency domain) [23, 94, 24, 96, 101, 102], square-sinc [98], exponential-Lorentzian [100, 101, 102, 99] and Gaussian-Gaussian [97] forms were demonstrated.

Third, pump and probe instantaneously excite and prepare molecules in the coherence state. This molecular coherence dephases eventually. The dephasing can be illustrated as exponential tale (usually in ps time scale) with a steep rise edge (usually in fs time scale), see dashed curves in Figure 4.8, on left column. The key idea is to catch, i.e., probe this coherence before it is too late. Thus, the probe cannot be delayed too much. Overlapping with the excitation pulses unfortunately also leads to overwhelming FWM background. The optimal probe delays are sketched in Figure 4.8, left column for different probe pulse shapes in time-domain. Among them, the most appropriate and shape-preserved one is the exponential-Lorentzian pulse, although its sharp spectral nature is sometimes suffered by its broadband tale-artifact. As seen from Figure 4.8, the square-sinc pulse, the same as for expontential-Lorentzian pulse, has a steep rise, and the sinc-square pulse has a first left node - all these features are conveniently optimize probe delay in such a way that the FWM contribution is minimized.

Fourth, the CARS enhancement at non-zero delay is obvious for the molecules with narrow band Raman lines in the case of, for example, substances in gas or liquid phase. However, as seen from Eq.(4.3) that for broader Raman lines, this effect is negligible. The examples are tissue, powder, and other soft matters. For heterogenous samples due to multiple scattering, fluorescence, and other additional processes the present technique can be suffered at certain degree. However, a tendency of improving signal-to-noise ratio is governed by the very same idea present here. For example, the single shot data of spores powder can still be discriminated from the heterogeneous background which were somewhat suppressed at the right probe delay and, perhaps, signal can also be enhanced simultaneously. Anyway, these points need further detailed experimental analysis. Enhancement is a more significant effect for substances in liquid or gas phase. For N_2 at room temperature, an observation

of the CARS enhancement at positive probe delay was reported in [120]. This is a high spectral resolution experiment using a 1-m spectrometer with a dispersion of 0.29 cm^{-1} per pixel of the CCD camera. The laser pulses are in picosecond time scale. The pump and Stokes pulses were approximately 100 ps generated by a regeneratively amplified mode-locked Nd:YAG laser in combination with a broadband dye laser centered at 633 nm. A precisely synchronized second regeneratively amplified Nd:YAG laser produced a narrowband probe beam at 532 nm. The results reproduced from [120] are shown in Figure 4.10 where CARS signal were recorded at each probe delay for three different peaks. The peaks correspond to the rotational quantum number J-specific Raman modes (J=8, 16, and 22). The decay of these coherence were measured in N_2 at room temperature. The J-specific exponential decay constants ($\tau_{8,16,22}$) were accurately found from the exponential fits in the tale parts of the observed data. The expected deviations between the threshold delay times for those peaks from the present theory were, however, measured inaccurately as in Figure 4.10. Note that enhancement is due to molecular coherence in unison as a result of collective phenomenon (below 200 ps) which is the case for decay of Raman modes in long delay (above 200 ps). The collective phenomenon in this case, thus, depend mostly on the excitation of pump and probe pulses.

Finally, let us discuss an impulsive CARS experiment representing the group that utilizes a narrowband probe and broadband excitations. Selm et al., in [98], used a mode-locked Er-fiber laser oscillator (40 MHz rep. rate) and the two parallel Er:fiber amplifiers at 1550 nm. The one branch delivered the broadband pulse (short as 11 fs in duration) that can excite the molecules in the sample substance impulsively. The other branch generates a probe pulse with a duration of 3 ps with a use of PPLN at 775 nm (second harmonic of the fundamental 1550 nm). This had a 200 fs fast rise time of the top-hat shape in time domain as in Figure 4.9 (b). The leading sharp
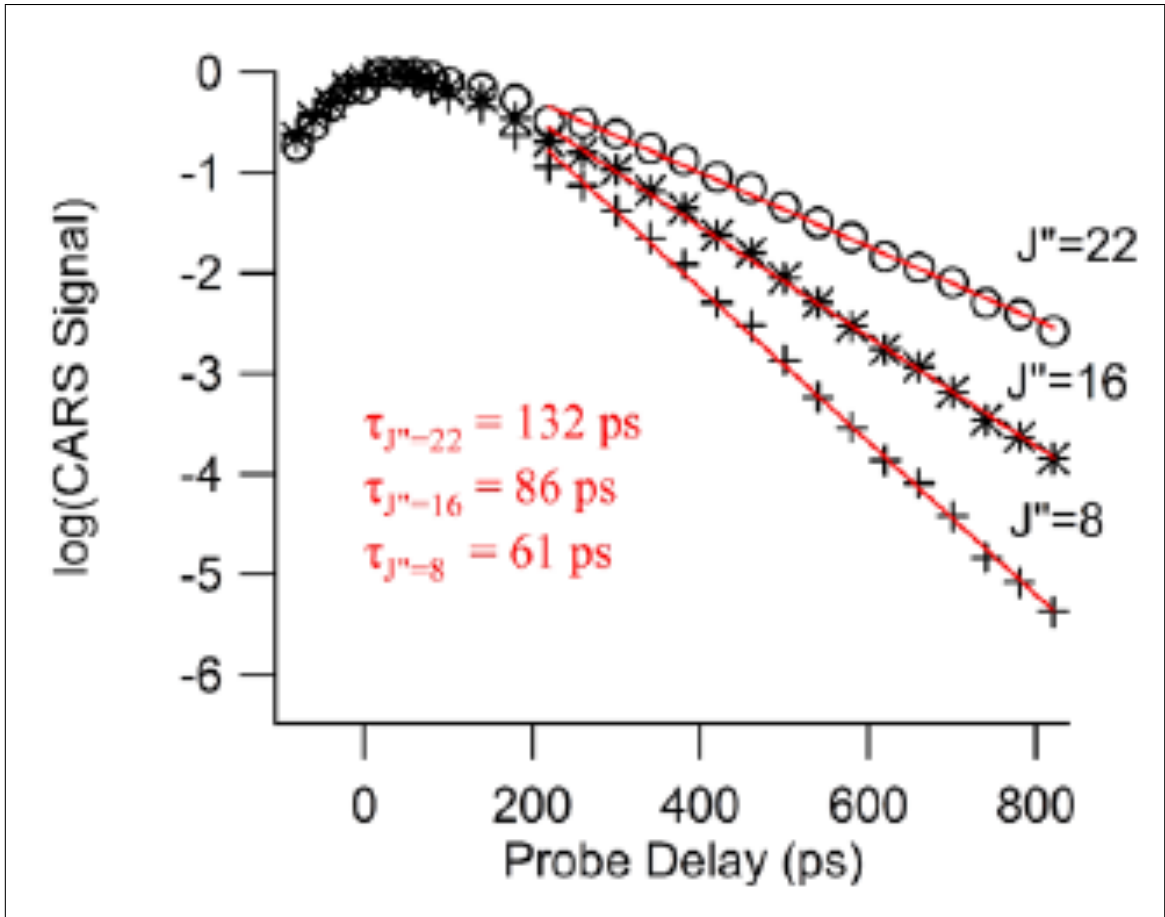
Figure 4.10: The results are reproduced from [120]. The CARS signals as functions of probe delay for three excited closely-spaced rotational Raman modes with $J = 8$, 16, and 22 of N_2 in gas-phase at room temperature. The maximum enhancements for these modes are at threshold delay time of approximately 50 ps. The exponential fits in the tale parts provides Raman modes' decay constants (or inverse of linewidths) to be $\tau_{8,16,22} = 61$, 86, and 132 ps.

edge of the (delayed) probe pulse can be aligned with respect to the excitation pulse for removal of non-resonant background. The main experimental result from [98] is reproduced in Figure 4.11 (a). As seen from figure, in the zero delay region, the CARS signal overwhelmed by the featureless non-resonant background. At the delay longer, the time-resolved excited Raman bands of a benonitrile liquid film. The 11 fs pulse allowed excitation of multiplex Raman peaks in the entire range from
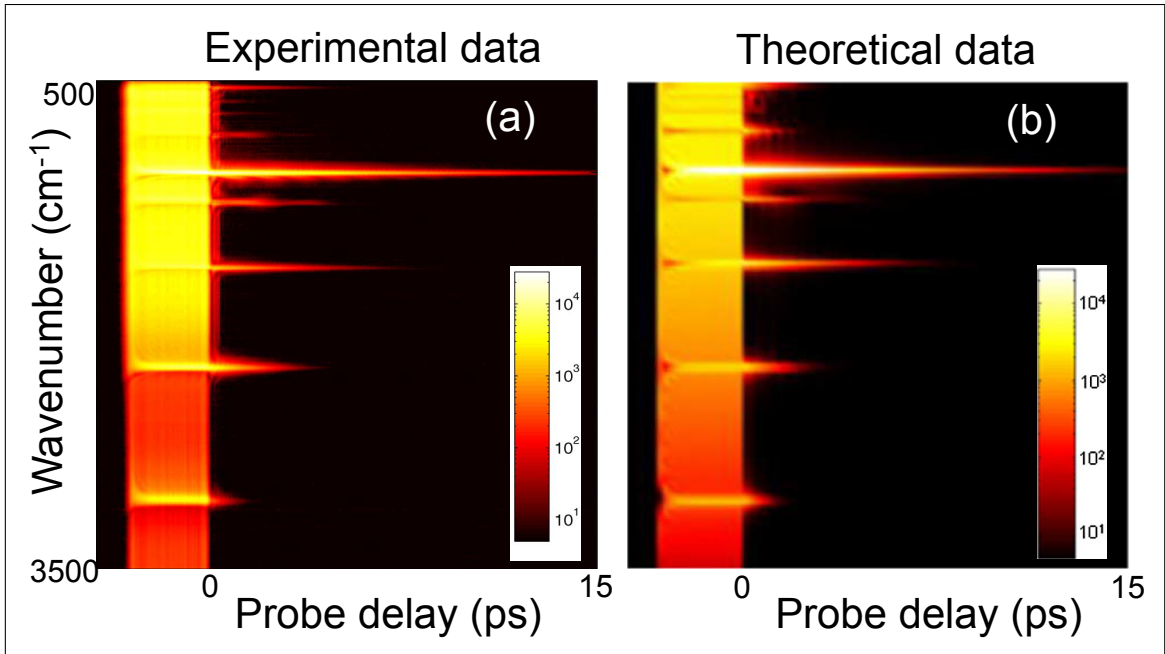
Figure 4.11: (a) The experimental data reproduced from [98]. (b) Simulations reproduced from [105]. Time-resolved impulsive CARS spectrograms for a liquid film of benzonitile.

500 to 3500 cm^{-1}. The theoretical comparison to this data was given in [105], see Figure 4.11(b). The theory for the impulsive CARS is developed in [105, 106], and its generalization is presented here.

Summary

This section presented a brief overview to the basics of coherent anti-Stokes Raman spectroscopy. First we introduced the CARS technique and its strengths and barriers. In particular, the experiments using combination of broadband and narrowband pulses were highlighted. Next, the application of the Gaussian ultrashort pulses as a practical elucidatory reconstruction tool to be used in the extraction of uncontaminated CARS signal from FWM background was analyzed in great detail. Namely, we presented the integral formulae for coherent anti-Stokes and Stokes Ra-

man scattering, and discussed the closed-form solutions, its complex error function, and the formula for maximum enhancement of the inferred pure coherent Raman spectra. The time-resolved coherent Stokes Raman scattering experimental observations were also quantitatively elucidated as an example. Moreover, various experimental realizations of narrowband probe pulses were illustratively explained. Finally, several experimental data were presented and discussed based on all Gaussian approach presented in this section. Understanding the essentials of coherent Raman spectroscopy promotes importance of a number of experiments including the ones utilizing a broadband excitation with a narrowband delayed probing for successful background suppression emphasized in this section.

COHERENT STOKES RAMAN SPECTROSCOPY OF PYRIDINE IN GAS-PHASE AT LOW TEMPERATURE *

In this section, coherent Stokes Raman spectroscopic data of pyridine in gas-phase are presented. Both time and frequency resolved (femtosecond and picosecond adaptive) coherent Raman spectroscopic technique demonstrates a measurement sensitivity reaching below 30 ppm pyridine molecules.

Introduction

Coherent anti-Stokes/Stokes Raman spectroscopy is a powerful tool, for example, in chemical sensing, molecular dynamics observations, and ro-vibrational spectroscopy. Since its first demonstration [74], it has been successfully applied in fields of study as diverse as remote sensing, combustion diagnostics, cell biology and plasma physics. Due to molecular coherence, Raman scattering efficiency can be enhanced by many orders of magnitude [94]. In coherent Stokes Raman scattering (CSRS) spectroscopy employed in this work. The molecules are put into coherent oscillations by a pair of preparation pulses, pump and Stokes. These macroscopic polarization oscillations of molecules lead to enhanced scattering of the probe photons. We studied the two excited Raman modes of ν_8 at 1030 cm^{-1} for the ring bend and ν_9 at 990 cm^{-1} for the ring breathing.

Experimental Setup

We employ a Coherent Inc., Ti-Sapphire-based regenerative amplifier system with 1 kHz repetition rate at 800 nm wavelength (maximum pulse energy 1 mJ/pulse,

pulse duration ∼ 40-50 fs). The generated CSRS signal, in transmission mode in the sample, is collected by a diffraction-grating spectrometer (Chromix-250is, Bruker optics) with a liquid nitrogen cooled CCD (Spec-10, Princeton Instruments)(see Figure 5.1).
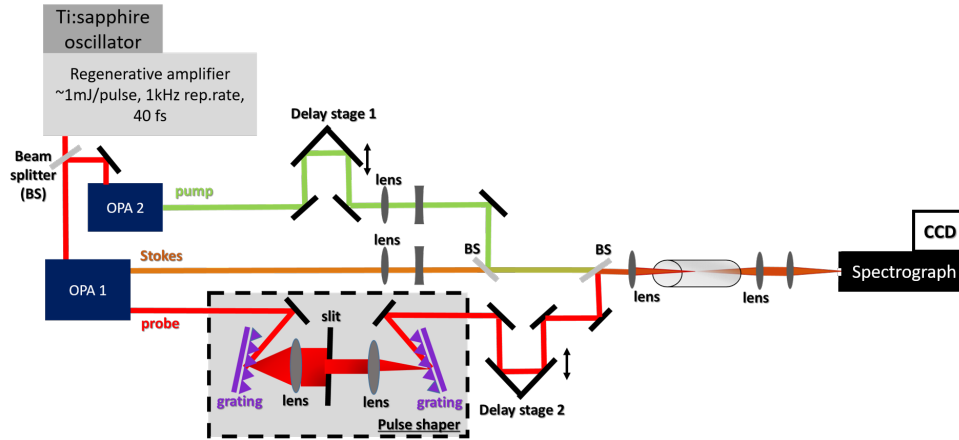
Figure 5.1: The experimental setup of a CARS system

The femtosecond system produces the three linearly polarized laser beams at preselected wavelengths. These are utilized as pump, Stokes, and probe. The probe pulse is guided through a home-made 4-f pulse shaper. An adjustable slit in the Fourier plane of spectrally-dispersed beam provides a narrowband probe. The probe and Stokes pulses are sent directly through designated delay lines and then all three colinear beams are focused on the sample. The delay stages are motorized, controlled by a PC and operated with 1 μm precision (Newport). We ran a couple of measurements for finding an optimal probe bandwidth which resolves the two excited Raman modes (39 cm^{-1} apart from each other) and the same time provides good signal to noise ratio. The dependence between the slit width of the pulse shaper

and the probe bandwidth was measured to be linear. Next, we investigated experimentally the CSRS concentration dependence. CSRS signal measured as pyridine concentration is changed by heating and cooling the cell (Figure 5.2). As expected,
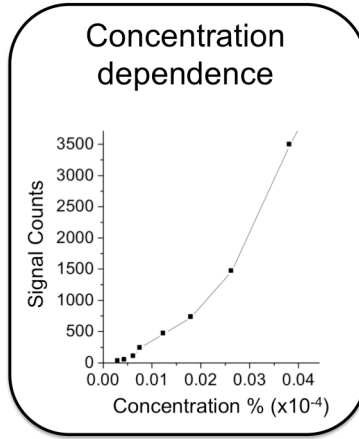
Figure 5.2: CSRS signal concentration dependence below 0.1% by varying temperature of the pyridine in gas-phase.

the nonlinear (quadratic) relationship was observed, particularly, in a region of concentration reached below 0.1%. During the experiment, the powers of the pump, Stokes, and probe were kept the same at 1.8 mW, 3.1 mW, and 1.5 mW, respectively. The employed femtosecond and picosecond adaptive CSRS technique can be best understood through its comparison with time-resolved CSRS. An illustrative transition from the conventional time-resolved CSRS measurement in pyridine to the frequency resolved (multiplex) CSRS by narrowing the bandwidth of the probe pulse from 300 cm^{-1} to 15 cm^{-1} is shown in Figure 5.3. A beating pattern between the two excited Raman modes of interest, 990 and 1030 cm^{-1}, transforms gradually into two spectrally resolved lines. A cross section of the spectrograms at the fixed positive delay gives a CSRS spectrum.
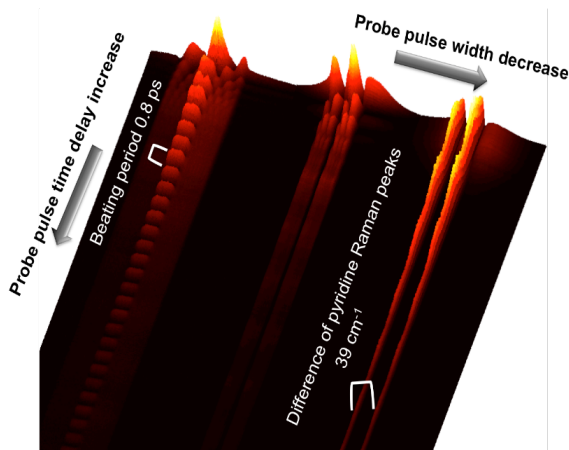
Figure 5.3: A transition from the traditional time-resolved CSRS to frequency resolved CSRS left to right the probe width changed from 300 to 15 cm^{-1}. A separation of the two Raman lines for pyridine is $39cm^{-1}$ and a corresponding beating period is 0.8 ps.

Results and Discussion

For lower concentration measurements, the cell needed to be cooled. The lowest stable cooling achieved in this experiment was about 4 Celsius. At this temperature, the pyridine concentration is estimated to be 28 ppm. In Figure 5.4, a single laser shot measurement is shown. It is worth to noting that the non-resonant background four-wave-mixing profile due to multiple off-resonant vibrational modes and instantaneous electric response is highly suppressed [23], due to the delayed probe. The sharp resolution of the Raman lines were obtained due to narrowband feature of the probe. The maximum enhancement of CSRS at the threshold probe delay is used [104]. In this experiment, overall 2000 counts were recorded, which suggested that we are able to push to sub-ppm sensitivity.

CSRS detection
of 28 ppm pyridine

39 cm^{-1}

1000 Counts
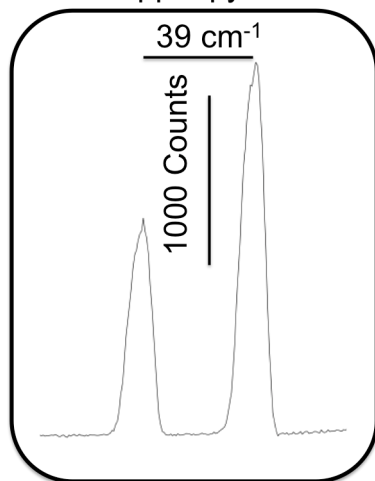
Figure 5.4: A single shot CSRS spectrum for 28 parts per million pyridine molecules. The powers of pump, Stokes and probe are 1.8 mW, 3.1 mW, and 2 mW, respectively, the acquisition time is 200 ms.

CONCLUSION

This work is mainly devoted to development of Raman spectroscopic techniques for in vivo detection of abiotic plant stress and animal diet prediction by their feces' Raman spectra. We demonstrated, for the first time, early detection of plant stress responses using *in vivo* Raman spectroscopic methods with improved sensitivity and the ability to interrogate individual stress-indicator pigment molecules simultaneously. The variations in the concentration levels of anthocyanins and photosynthetic carotenoids in coleus plants were observed across abiotic stresses including high salinity, drought, cold, and excess light. These changes over time post-stress induction provides Raman spectroscopy as a method of accurate measurement of these molecules, while indicative of the functional relationship of these pigments in response to excessive ROS during abiotic stress. This work furthers our understanding of plant physiology by detecting a novel negative correlation in the levels of anthocyanins and carotenoids during the stress response. The short term response across multiple abiotic stresses holds promise for a near ubiquitous method of abiotic stress detection. Finally, our proposed portable system has the capability to become mobile and automated to allow for increased utility in precision agricultural applications both for breeders and commercial producers. The traditional chemical analytical extraction also validated the existence of the concentration changes either, in total anthocyanins or carotenoids. In general, the Raman technique could be a cheap, rapid, non-destructive, and alternative to chemical analysis. Since it is *in vivo*, it detects changes of these molecules over time from one plant which is impossible in destructive chemical analysis. In the next study, we showed that f.NIRS has the potential to, at a minimum, predict high and low consumers of chemically

defended plants such as mesquite that are only consumed in small amounts. This information can be used to help select animals that have a higher intake of these plants and thus have a greater potential to more effectively utilize the forage resource in areas where species such as mesquite are abundant. This is the first study to demonstrate that Raman spectroscopy has the potential for discriminating among animals that are consuming different diets. Because in contrast to NIR, water does not affect Raman and because field friendly, hand held Raman spectrometers, such as the one used in this study, are readily available, this technology has a great potential for ecological field studies. NIRS spectroscopy has shown great potential in ecological studies [53, 66]. We believe that Raman spectroscopy has a similar potential and deserves further investigation as a quantitative technique in ecological field studies. In the section 4, we presented a brief overview to the basics of coherent anti-Stokes Raman spectroscopy. First we introduced the CARS technique and its strengths and barriers. In particular, the experiments using combination of broadband and narrowband pulses were highlighted. Next, the application of the Gaussian ultrashort pulses as a practical elucidatory reconstruction tool to be used in the extraction of uncontaminated CARS signal from FWM background was analyzed in great detail. Namely, we presented the integral formulae for coherent anti-Stokes and Stokes Raman scattering, and discussed the closed-form solutions, its complex error function, and the formula for maximum enhancement of the inferred pure coherent Raman spectra. The time-resolved coherent Stokes Raman scattering experimental observations were also quantitatively elucidated as an example. Moreover, various experimental realizations of narrowband probe pulses were illustratively explained. Finally, several experimental data were presented and discussed based on all Gaussian approach presented in this section. Understanding the essentials of coherent Raman spectroscopy promotes importance of a number of experiments including the ones

utilizing a broadband excitation with a narrowband delayed probing for successful background suppression emphasized in this section.

REFERENCES

[1] C.V. Raman and K. Krishnan, "A new type of secondary radiation". Nature, **121**, 501-502 (1928).

[2] H.A. Szymanski, *Raman Spectroscopy: Theory and Practice.* (Plenum Press, 1967).

[3] J.D. Ingle Jr, and S.R. Crouch, *Spectrochemical Analysis.* (Prentice Hall College Book Division, 1988)

[4] N.B. Colthup, L. H. Daly, S. E. Wiberley. 1990. *Introduction to Infrared and Raman spectroscopy*, 3rd ed. (Academic Press, 1990).

[5] L.D.S. Yadav, *Organic spectroscopy.* (Kluwer Academic Publisher, 2005).

[6] G. Turrell, J. Corset, *Raman microscopy: Developments and Applications.* (Academic Press, 1996).

[7] M. Delhaye, P. Dhamelincourt, "Raman microprobe and microscope with laser excitation". J. Raman Spectrosc. **3**, 33-43, 1975.

[8] T. Miura and G. Thomas Jr., *Introduction to Biophysical Methods for Protein and Nucleic Acid Research: Optical and Vibrational Spectroscopic Methods.* (Academic Press, 1995).

[9] M.S. Braiman, *Vibrational Spectroscopy of Biological and Polymeric Materials.* (CRC Press, 2006).

[10] T.R. Hata, T.A. Scholz, et al., "Non-invasive Raman spectroscopic detection of carotenoids in human skin." J. Investigative Dermatology **115**, 441-448 (2000).

[11] N. Gierlinger , T. Keplinger, M. Harrington, "Imaging of plant cell walls by confocal Raman microscopy". Nature Protocols, **7**, 1694-1708 (2012).

[12] N.E. Borlaug, "Ending world hunger. The promise of biotechnology and the threat of antiscience zealotry". Plant Physiol., **124**, 487-490 (2000).

[13] D. Tilman, J. Fargione, B. Wolff, C. D'Antonio, A. Dobson, R. Howarth, D. Schindler, W. H. Schlesinger, D. Simberloff, D. Swackhamer,"Forecasting agriculturally driven global environmental change". Science, **292**, 281-284.

[14] F. Fiorani, U. Schurr, "Future scenarios for plant phenotyping". Annu. Rev. Plant Biol., **64**, 267-291 (2013).

[15] M.A.K. Jansen, V. Gaba, B.M. Greenberg, "Higher plants and UV-B radiation: balancing damage, repair and acclimation". Trends in plant science, **3**, 131-135 (1998).

[16] L. Bernstein, "Effects of salinity and sodicity on plant growth". Annu.Rev. Phytopath., **13**, 295-312 (1975).

[17] A. Gitelson, M. Merziyak, "Signature analysis of leaf reflectance spectra: algorithm development for remote sensing of chlorophyll". J. Plant Physiol., **148**, 494-500 (1996).

[18] H.M. Kalaji, K. Bosa, K. Janusz, Z. Hossain, "Chlorophyll a fluorescence- a useful tool for the early detection of temperature stress in spring barley". J Integr Biol., **15**, 925-934 (2011).

[19] S. Zia, G. Romano, W. Spreer, C. Sanchez, J. Cairns, J. L. Araus, J. Muller, "Infrared thermal imaging as a rapid tool for identifying water-stress tolerant maize genotypes of different phenology". J. Agron. Crop Sci. ,**199**, 75-84 (2013).

[20] N. Born, D. Behringer, S. Liepelt, S. Beyer, M. Schwerdtfeger, B. Ziegenhagen, M. Koch, "Monitoring plant drought stress response using terahertz time-domain spectroscopy". Plant Physiol., **164**, 1571-1577 (2014).

[21] J. Behmann, J. Steinrᬌcken, L. Plᬌmer, "Detection of early plant stress responses in hyperspectral images". ISPRS J. Photogramm. Remote Sens., **93**, 98-111 (2014).

[22] K.E. Shafer-Peltier, A.S. Haka, M. Fitzmaurice, J. Crowe, J. Myles, R.R. Dasari, M.S. Feld, "Raman micro spectroscopic model of human breast tissue: implications for breast cancer diagnosis in vivo". J. Raman Spectrosc., **33**, 552-563 (2002).

[23] D. Pestov, R.K. Murawski, G.O. Ariunbold, X. Wang, M. Zhi, A.V. Sokolov, V.A. Sautenkov, Yu.V. Rostovtsev, A. Dogariu, Yu Huang, and M.O. Scully,"Optimizing the laser-pulse configuration for coherent Raman spectroscopy". Science **316**, 265-268 (2007).

[24] D. Pestov, X.Wang, G.O. Ariunbold, R.K. Murawski, V.A. Sautenkov, A. Dogariu, A.V. Sokolov, and M.O. Scully, "Single-shot detection of bacterial endospores via coherent Raman spectroscopy". Proc Natl Acad Sci USA, **105**, 422-427 (2008).

[25] D. Yang, Y. Ying, "Applications of Raman spectroscopy in agricultural products and food analysis: a review". Appl. Spectrosc. Rev.,**46**, 539-560 (2011).

[26] L. Chalker-Scott, "Environmental significance of anthocyanins in plant stress responses". Photochem. Photobiol., **70**, 1-9 (1999).

[27] K. Apel, H. Hirt,"Reactive oxygen species: metabolism, oxidative stress, and signal transduction". Annu. Rev. Plant Biol., **55**, 373-399 (2004).

[28] F. Ramel, S. Birtic, C. Ginies, L. Soubigou-Taconnat, C. Triantaphylides, M. Havaux, "Carotenoid oxidation products are stress signals that mediate gene responses to singlet oxygen in plants". Proc Natl Acad Sci USA, **109**, 5535-5540 (2012).

[29] M. Havaux, "Carotenoid oxidation products as stress signals in plants". The Plant Journal, **79**, 597-606 (2013).

[30] R.R. Wise, A.W. Naylor, "Chilling-enhanced photooxidation evidence for the role of singlet oxygen and superoxide in the breakdown of pigments and endogenous antioxidants". Plant Physiol., **83**, 278-282 (1987).

[31] B.F. Kennedy, L.F. De Filippis, "Physiological and oxidative response to NaCl of the salt tolerant Grevillea and the salt sensitive Grevillea arenaria". J. Plant Physiol., **155**, 746-754 (1999).

[32] N. Kovinich, G. Kayanja, A. Chanoca, K. Riedl, M. Otegui, E. Grotewold, "Not all anthocyanins are born equal: distinct patterns induced by stress in Arabidopsis". Planta., **240**, 931-940, (2014).

[33] p. Nguyen, V. Cin, "The role of light on foliage colour development in coleus (Solenostemon scutellarioides (L.) Codd)". Plant Physiol. Biochem., **47**, 934-945 (2009).

[34] D. Treutter, "Significance of flavonoids in plant resistance and enhancement of their biosynthesis". Plant Biol., **7**, 581-591 (2005).

[35] E. Petrussa, E. Braidot, M. Zancani, C. Peresson, A. Bertolini, S. Patui and A. Vianello, "Plant flavonoids-biosynthesis, transport and involvement in stress responses". Int. J. Mol. Sci., **14**, 14950-14973 (2013).

[36] A. Henry, S. Chopra, D. Clark, J. Lynch, "Responses to low phosphorus in high and low foliar anthocyanin coleus (Solenostemon scutellarioides) and maize (Zea mays)". Funct. Plant Biol., **39**, 255-265 (2012).

[37] C. Lieber, A. Mahadevan-Jansen, "Automated method for subtraction of fluorescence from biological Raman spectra". Appl. Spectrosc., **57**, 1363-1367 (2003).

[38] H. K. Lightenthaler, C. Buschmann, "Extraction of Photosynthetic Tissues: Chlorophylls and Caroteoids". Current protocols in food analytical chemistry, **55**, F4.2.1-F4.2.6, (2001).

[39] H.K. Lightenthaler, C. Buschmann, "Chlorophylls and carotenoids: measurement and characterization by UV-VIS spectroscopy". Current Protocols in Food Analyt. Chem., **55**, F4.3.1-F4.3.8, (2001).

[40] M. Baranska, M. Roman, J. Dobrowolski, H. Schulz, R. Baranski, "Recent advances in Raman analysis of plants: alkaloids, carotenoids, and polyacetylenes". Current Analyt. Chem., **9**,108-127 (2013).

[41] H. Schulz, M. Baranska, R. Baranski, "Potential of NIR-FT-Raman spectroscopy in natural carotenoid analysis". Biopolymers, **77**, 212-221 (2005).

[42] R. Brouillard, "The in vivo expression of anthocyanin colour in plants". Phytochem., **22**, 1311-1323 (1983).

[43] J. Merlin, A. Statoua, J. Cornard, M. Saidi-Idrissi, R. Brouillard, "Resonance Raman spectroscopic studies of anthocyanins and anthocyanidins in aqueous solutions". Phytochem., **35**,227-232, (1994).

[44] M. Buchweitz, G. Gudi, R. Carle, D.R. Kammerer, H. Schulz, "Systematic investigations of anthocyanin-metal interactions by Raman spectroscopy". J. Raman Spectr., **43**, 2001-2007 (2012).

[45] A. Haka, K.E. Shafer-Peltier, M. Fitzmaurice, J. Crowe, R.R. Dasari, M.S. Feld , "Diagnosing breast cancer by using Raman spectroscopy". Proc Natl Acad Sci USA, **102**, 12371-12376 (2005)

[46] Achakzai, A. K. K., P. Achakzai, A. Masood, S. A. Kayani, and R. B. Tareen, "Response of plant parts and age on the distribution of secondary metabolites on plants found in Quetta". Pakistan J. Botany. **41**, 2129-2135 (2009).

[47] A. Anderson, *The Raman effect. Vol. 1, Principles.*(Marcel Dekker Inc., 1973).

[48] U.P. Agarwal, "An overview of Raman spectroscopy as applied to lignocellulosic materials", Advances in Lignocellulosic Characterization, Chap. 9. Ed. D.S. Argyropoulos (TAPPI Press, 1999).

[49] R. Baptista and K. L. Launchbaugh, "Nutritive value and aversion of honey mesquite leaves to sheep". J. Range Manage. **54**, 82-88 (2001).

[50] L.M. Chen, R.H. Wilson and M.C. McCann, "Investigation of macromolecule orientation in dry and hydrated walls of single onion epidermal cells by FT-IR microspectroscopy". J. Molec. Struct., **408**, 257-260 (1997).

[51] N.B. Colthup, L. H. Daly, S. E. Wiberley, *Introduction to Infrared and Raman spectroscopy.* 3rd ed. (Academic Press, 1990).

[52] A. Copikova, J. Matejka, P. Machovic, and V. Machovic, "Fourier transform Raman and infrared spectroscopy of pectins". Carbohydr. Polym., **54**, 97-106 (2003).

[53] W.J. Foley, A. McIlwee, I. Lawler, L. Aragones, A.P. Woolnough and N. Berding, "Ecological applications of near infrared reflectance spectroscopy: a tool for rapid, cost-effective prediction of the composition of plant and animal tissues and aspects of animal performance". Oecologia.,**116**, 293-305 (1998).

[54] D.M. Haaland, Thomas, E.V., "Partial least squares methods for spectral analysis. 1. Relation to other quantitative calibration methods and the extraction of qualitative information". Anal. Chem., 601193-1202, (1988).

[55] B.H. Holder, "Characterization of starch by vibrational spectroscopy". thesis, UNL library, (2012).

[56] M. Kacurikova, N. Wellner, A. Ebringerova, Z. Hromidkova, R.H. Wilson, and P.S. Belton,"Characterization of xylan-type polysaccharides and associated cell wall components by FT-IR and FT-Raman spectroscopies". Food hydrocoll., **13**, 35-41 (1998).

[57] K.L. Larsen and S. Barsberg. "Theoretical and Raman spectroscopic studies of phenolic lignin model monomers". J. Phys. Chem. B, **114**, 8009-8021 (2010).

[58] M. Gonzalez,"Use of honey mesquite to enhance sustainability of southwestern range lands". MS Thesis, New Mexico State University,94 p,(2000).

[59] W. Saeys, A.M. Mouazen and H. Ramon, "Potential for onsite and online analysis of pig manure using visible and near infrared reflectance spectroscopy", Biosystems Eng.,**91**, 393-402 (2005).

[60] A. Savitzk and A.M.J. Golay, "Smoothing and differentiation of data by simplified least squares procedures". Anal. Chem., **36**, 1627-1639 (1964).

[61] K. Schenzel and S. Fisher, "NIR FT Raman spectroscopy- a rapid analytical tool for detecting the transformation of cellulose polymorphs". Cellulose, **8**, 49-57 (2001).

[62] H. Schultz and M. Baranska, "Identification and quantification of valuable plant substances by IR and Raman spectroscopy". Vib. Spectrosc., **43**, 13-25 (2007).

[63] H.W. Sieler, Y.Ozaki, S.Kawata, and H.M.Heise, *Near-Infrared spectroscopy principles, Instruments, Applications.* 1st Edn. (Wiley-VCH Verlag GmbH, 2002).

[64] L. Sun, C. Li, Z. Xue , B.A. Simmons, and S. Singh, "Unveiling high resolution, tissue specific dynamic changes in corn stover during ionic liquid pretreatment". RSC Adv., **3**, 2017-2027, (2013).

[65] P.J. Van Soest, *Nutritional Ecology of the Ruminant.* (O and Books Inc.,1982).

[66] C.K. Vance, D.R. Tolleson, K. Kinoshita, J. Rodriguez and W.J. Foley, "Near infrared spectroscopy in wildlife and biodiversity". J. Near Infrared Spectrosc., **24**, 1-25 (2016).

[67] J.W. Walker, E.J. Campbell, R.W. Kott, S.Y. Landau, C.J. Lupton, C.B. Scott, L. Surber, C.A. Taylor, Jr., and W.R. Whitworth, "Fecal NIRS for predicting botanical composition of herbivore diets", in: J. Walker, and D. Tolleson, (eds). Shining light on manure improves livestock and land management. Texas AgriLife Resarch Tech. Bull. SANG-2010-0250. Texas AgriLife Research, San Angelo, TX. (2010).

[68] J.W. Walker, D.H. Clark, and S.D. McCoy, "Fecal NIRS for predicting percent leafy spurge in diets". J. Range. Manage., **51**, 450-455 (1998).

[69] J.W. Walker, S.D. McCoy, K.L. Launchbaugh, M.J. Fraker, J. Powell, "Calibrating fecal NIRS equations for predicting botanical composition of diets". J. Range Manage., **55**, 374-382 (2002).

[70] J.H. Wiley, and R.H. Atalla, "Band assignments in the Raman spectra of celluloses". Carbohydr. Res., **160**, 113-129 (1987).

[71] P. Williams and K. Norris, "Near-infrared Technology in the Agricultural and Food Industries". Second Edition American Association of Cereal Chemist, Inc. St. Paul, MN.(2001).

[72] B.K. Witmore,"Potential of biological control of honey mesquite and its use as a forage resource for livestock". [M. S. Thesis]. Las Cruces, NM: New Mexico State University. 147 p.(2009).

[73] J. Workman and L. Weyer , *Practical Guide to Interpretive Near-Infrared Spectroscopy.* (CRC Press, 2007).

[74] P.D. Maker, and R.W. Terhune, "Study of optical effects due to an induced polarization third order in the electric field strength", Phys. Rev., **148**, 990, (1966)

[75] M.D. Duncan, J. Reintjes, and T.J. Manuccia, "Scanning coherent anti-Stokes microscope", Opt Lett,**7**, 350-352 (1982).

[76] A. Zumbusch, G.R. Holtom, and X.S. Xie, "Three-dimensional vibrational imaging by coherent anti-Stokes Raman scattering", Phys. Rev. Lett., **82**, 4142-4145 (1999).

[77] S. Roy, J.R. Gord, and A.K. Patnaik, "Recent advances in coherent anti-Stokes Raman scattering spectroscopy: Fundamental developments and applications in reacting flows", Prog. Energ. Combust, **36**,280-306 (2010).

[78] W.M. Tolles, J.W. Nibler, J.R. McDonald, and A.B. Harvey, "A review of the theory and application of coherent anti-Stokes Raman spectroscopy", Appl. Spectrosc., **31**, 253-271 (1977).

[79] A. M. Zheltikov, "Coherent anti-Stokes Raman scattering: from proof-of-the-principle experiments to femtosecond CARS and higher order wave-mixing generalizations", J. Raman Spectrosc,**31**, 653-667 (2000).

[80] 3. L.G.Rodriguez,Stephen Lockett, Gary R. Holtom, "Coherent anti-Stokes Raman scattering microscopy: A biological review", Cytometry Part A,**69A**, 779-791 (2006).

[81] C. L. Evans and X. S. Xie, "Coherent Anti-Stokes Raman Scattering Microscopy: Chemical Imaging for biology and medicine", Annu. Rev. Anal. Chem., **1** 883-909, (2008).

[82] Y. Silberberg, "Quantum coherent control for nonlinear spectroscopy and microscopy", Annu. Rev. Phys. Chem., **60**, 277-292 (2009).

[83] Fouad El-Diasty, "Coherent anti-Stokes Raman scattering: Spectroscopy and microscopy", Vibrational Spectroscopy,**55**, 1-37 (2011).

[84] G. Mogilevsky, L.Borland, M.Brickhouse, and A.W. Fountain III, "Raman spectroscopy for homeland security applications", International J. Spec., **2012**, 808079 (2012).

83

[85] D.I. Ellis, D.P. Cowcher, L. Ashton, S. O'Hagan, and R. Goodacre, "Illuminating disease and enlightening biomedicine: Raman spectroscopy as a diagnostic tool", Analyst, **138**, 3871-3884 (2013).

[86] W.R. Lempert and I.V. Adamovich, "Coherent anti-Stokes Raman scattering and spontaneous Raman scattering diagnostics of nonequilibrium plasmas and flows", J. Phys. D: Appl. Phys. **47** 433001 (2014).

[87] Ji-X. Cheng, and X.S. Xie, *Coherent Raman scattering microscopy*, (CRC press, 2013).

[88] C.H. Camp Jr, and M. Cicerone, "Chemically selective bioimaging with coherent Raman scattering", Nat Photonics, **9**, 295-305 (2015).

[89] L. A. Austin, and S. Osseiran, "Raman technologies in cancer diagnostics", Analyst, 2016 (2015).

[90] C. Krafft, I.W. Schie, T. Meyer, and M. Schmidth, "Developments in spontaneous and coherent Raman scattering microscopic imaging for biomedical applications", Chem. Soc. Rev., 2016 (2015).

[91] R. M. Goodhead, J. Moger, T.S. Galloway, and C.R. Tyler, "Tracing engineered nanomaterials in biological tissues using coherent anti-stokes microscopy- A critical review", Nanotoxicology, **9**, 928-939 (2015)

[92] K. Kong, C. Kendall, N. Stone, and I. Notinger, "Raman spectroscopy for medical diagnostics - From in-vitro biolfluid assays to in-vivo cancer detection", Adv. Drug Deliv. Rev. **89**, 121-134 (2015).

[93] Y. Shen, D.V. Voronine, A.V. Sokolov and M.O. Scully, "A versatile setup using femtosecond adaptive spectroscopic techniques for coherent anti-Stokes Raman scattering", Rev. Sci. Instrum., **86**, 083107 (2015).

[94] D. Pestov, G.O. Ariunbold, X. Wang, R.K. Murawski, V.A. Sautenkov, A.V. Sokolov, and M.O. Scully, "Coherent versus incoherent Raman scattering: Molecular coherence excitation and measurement", Opt Lett, **32**,1725-1727 (2007).

[95] H. Kano, and H. Hamaguchi, "Dispersion-compensated supercontinuum generation for ultrabroadband multiplex coherent anti-Stokes Raman scattering spectroscopy", J. Raman Spectrosc., **37**, 411-415 (2006).

[96] B.D. Prince, A. Chakraborty, B.M. Prince, H.U. Stauffer "Development of simultaneous frequency-and time-resolved coherent anti-Stokes Raman scattering for ultrafast detection of molecular Raman spectra", J. Chem. Phys., **125**, 44502 (2006).

[97] J. Peng, D. Pestov, M.O. Scully, and A.V. Sokolov, "Simple setup for hybrid coherent Raman microspectroscopy", J. Raman Spectrosc., **40**, 795-799 (2009).

[98] R. Selm, M. Winterhalder, A. Zumbusch, G. Krauss, T. Hanke, A. Sell, and A. Leitenstorfer, "Ultrabroadband background-free coherent anti-Stokes Raman scattering microscopy based on a compact Er:fiber laser system", Opt Lett, **35**, 3282-3284 (2010).

[99] S.O. Konorov, M.W. Blades, and R.F. Turner, "Lorentzian amplitude and phase pulse shaping for nonresonant background suppression and enhanced spectral resolution in coherent anti-Stokes Raman scattering spectroscopy and microscopy", Appl Spectrosc, **64**, 767-774 (2010).

[100] V. Kumar,R. Osellame, R. Ramponi, G. Cerullo, and M. Marangoni, "Background-free broadband CARS spectroscopy from a 1 MHz ytterbium laser", Opt Lett, **19**, 15143-15148 (2011).

[101] H. Stauffer, J.D. Miller, S. Roy, J.R. Gord, and T.R. Meyer, "Communication: Hybrid femtosecond/picosecond rotational coherent anti-Stokes Raman scattering thermometry using a narrowband time-asymmetric probe pulse", J Chem Phys, **136**, 111101 (2012).

[102] H. Stauffer, J.D. Miller, M.N. Slipchenko, T.R. Meyer, B.D. Prince, S. Roy, and J.R. Gord, "Time-and frequency-dependent model of time-resolved coherent anti-Stokes Raman scattering (CARS) with a picosecond-duration probe pulse", J.Chem. Phys., **140**, 024316 (2014).

[103] M.O. Scully, G.W. Kattawar, R.P. Lucht, T.Opratrny, H.Pilloff, A.Rebane, A.V. Sokolov, and M.S. Zubairy, "FAST CARS: Engineering a laser spectroscopic technique for rapid identification of bacterial spores", PNAS, **99**, 10994-11001 (2002).

[104] G.O. Ariunbold and N. Altangerel, "Quantitative interpretation of time-resolved coherent anti-Stokes Raman spectroscopy with all Gaussian pulses", J. Raman Spectrosc., 2016.

[105] M. Marrocco, Time-domain coherent anti-Stokes Raman scattering in terms of the time-delayed Yuratich equation, Opt. Lett., **39**, 4831-4834 (2014).

[106] M.Marrocco, Closed-form solutions of coherent anti-Stokes Raman signals generated by means of time asymmetric probe pulses, J. Raman Spectrosc., **46**, 683-690 (2015).

[107] Y.J. Lee, S.H. Parekh, Y.H. Kim, and M.T. Cicerone, "Optimized continuum from a photonic crystal fiber for broadband time-resolved coherent anti-Stokes Raman scattering", Opt. Express, **18**, 4371-4379 (2010).

[108] S. Mukamel, *Principal of nonlinear optical spectroscopy*, (Oxford University Press, 1995).

[109] G. He, *Nonlinear optics and photonics*, (Oxford University Press, 2015).

[110] G.L. Eesley, *Coherent Raman Spectroscopy*, (Pergamon Press, 1981).

[111] M.A. Yuratich, "Effects of laser linewidth on coherent anti-Stokes Raman spectroscopy", Mol Phys, **38**, 625-655 (1979).

[112] N. Dudovich, D. Oron, and Y. Silberberg, "Single-pulse coherently controlled nonlinear Raman spectroscopy and microscopy", Lett. Nat., **418**, 512-514 (2002).

[113] D. Oron, N.Dudovich, and Y. Silberberg, "Femtosecond phase-and-polarization control for background-free coherent anti-Stokes Raman scattering microscopy, Phys. Rev. Lett., **90**, 213902 (2003).

[114] V. N. Faddeeva, and N. N. Terent'ev, "Tables of values of the function $w(z) = \exp(-z^2)(1 + 2i/\sqrt{\pi} \int_0^z \exp(t^2)\mathrm{d}t)$ for complex argument", Gosud. Izdat. Teh-Teor. Lit.,(1954).

[115] M.R. Zaghloul, and A.N. Ali, "ACM Transactions on Mathematical Software", **38**, 15 (2011).

[116] S.M. Abrarov, and B.M. Quine, "Accurate Approximations for the Complex error function with small imaginary argument", J. Math. Res., **7**, 44-53(2015).

[117] Y. Liu, Y.J. Lee, and M.T. Cicerone, "Broadband CARS spectral phase retrieval using time-domain Kramers-Kronig transform", Opt. Lett., **34**, 1363-1365 (2009).

[118] C.H. Camp, Y.J. Lee, J.M. Heddleston, C.M. Hartshorn, A.R.H. Walker, J.N. Rich, J.D. Lathia, and M.T. Cicerone, "High-speed coherent Raman fingerprint imaging of biological tissues", Nat. Photonics, **8**, 627-634 (2014).

[119] S. Roy, P.S. Hsu, N. Jiang, J.R. Gord, W.D. Kulatilaka, H.U. Stauffer, and J.R. Gord, "Direct measurements of collisionally broadened Raman linewidths of CO2 S-branch transitions.", J. Chem. Phys. **138**, 024201 (2013).

[120] C.J. Kleiwer, A. Bohlin, E. Nordström, B.D. Patterson, P.E. Bengtsson, and T.B. Settersten, "Time-domain measurements of S-branch N_2 Raman linewidths using picosecond pure rotational coherent anti-Stokes Raman spectroscopy", Appl. Phys. B **108**, 419 (2012).

[121] L.A. Carreira, L.P. Goss, and T.B. Malloy, "Comparison of the coherent anti-Stokes and coherent Stokes Raman line shapes of the v_1 line of β-carotene near a one photon resonance", J. Chem. Phys., **69**, 855 (1978).

[122] I. Tehver, H. Kaasik, and V. Hiznyakov, "Excitation profiles of resonant coherent Raman scattering by impurity molecules", J. Raman Spectrosc., **42**, 1958-1962 (2011).

[123] R. Leonhardt, W. Holzapfel, W. Zinth, and W. Kaiser, "Terahertz beats of vibrational modes studied by femtosecond coherent Raman spectroscopy", Revue Phys. Appl., **22**, 1735-1741 (1987).

[124] W. Zinth, and W. Kaiser, "Ultrafast coherent Raman spectroscopy", in proceedings of Lasers and Synergetics, R. Graham, A. Wunderlin ed. (Springer-Verlag 1987).